catalysts

MDPI

Article

Thermally Exfoliated g-C_3N_4/$Ti_3C_2T_x$ MXene Schottky Junctions as Photocatalysts for the Removal of Valsartan from Aquatic Environments

Christos Lykos and Ioannis Konstantinou *

Department of Chemistry, University of Ioannina, 45110 Ioannina, Greece; c.lykos93@gmail.com
* Correspondence: iokonst@uoi.gr

Abstract

In recent years, graphitic carbon nitride (g-C_3N_4) has gained considerable ground in the field of heterogeneous photocatalysis for the abatement of emerging contaminants from aqueous environments. Nonetheless, certain limitations, including a small surface area and a high recombination rate, limit its photocatalytic efficacy. In this study, g-C_3N_4 was synthesized from urea and then underwent thermal exfoliation. A portion of the exfoliated material was subsequently subjected to protonation via acid treatment, and both protonated and non-protonated variants of exfoliated g-C_3N_4 were combined with small amounts of $Ti_3C_2T_x$ MXene. The morphology, chemical structure, and optical properties of the synthesized materials were examined using various characterization techniques. Additionally, their photocatalytic performance was evaluated through laboratory tests using the commonly detected anti-hypertensive drug valsartan as a model pollutant. The degradation kinetics of valsartan revealed that combining 1% $Ti_3C_2T_x$ MXene with exfoliated g-C_3N_4 (both protonated and non-protonated) achieves optimal removal. Notably, the composite material 1%-pCNMX (protonated variant) displayed a 20% higher removal kinetic rate than unmodified exfoliated g-C_3N_4, removing a higher quantity of valsartan within the same time frame. Furthermore, all protonated composites proved more effective in degrading valsartan than their non-protonated counterparts, demonstrating the positive impact of acid treatment. The improved photocatalytic activity was attributed to the successful formation of Schottky junctions between g-C_3N_4 and $Ti_3C_2T_x$, which reduced the recombination rate of photogenerated charge carriers.

Keywords: Schottky junctions; g-C_3N_4; $Ti_3C_2T_x$; MXenes; photocatalysis; valsartan

check for updates

Academic Editor: Francisco Javier Rivas Toledo

Received: 3 August 2025
Revised: 13 September 2025
Accepted: 15 September 2025
Published: 18 September 2025

Citation: Lykos, C.; Konstantinou, I. Thermally Exfoliated g-C_3N_4/$Ti_3C_2T_x$ MXene Schottky Junctions as Photocatalysts for the Removal of Valsartan from Aquatic Environments. *Catalysts* **2025**, *15*, 909. https://doi.org/10.3390/catal15090909

Copyright: © 2025 by the authors. Licensee MDPI, Basel, Switzerland. This article is an open access article distributed under the terms and conditions of the Creative Commons Attribution (CC BY) license (https://creativecommons.org/licenses/by/4.0/).

1. Introduction

Extensive water pollution resulting from rapid industrialization and urban growth poses a significant challenge in the modern era due to the scarcity of clean water resources [1,2]. According to numerous reports, this issue is further exacerbated by the introduction and accumulation of various compounds, known as emerging contaminants (ECs), in the aquatic environment (e.g., pharmaceuticals and pesticides) [3,4]. Over the past few years, many studies have emphasized that ECs predominantly enter the aquatic environment through wastewater treatment plant (WWTP) effluents due to the inadequacy of these facilities in effectively eliminating them via conventional methods [5–7]. Therefore, there is a growing necessity for the development of non-conventional wastewater treatment methodologies capable of eliminating ECs in WWTPs, thus limiting their release.

Advanced oxidation processes (AOPs) have gained substantial interest in the field of wastewater treatment due to their attractive features, such as a small environmental footprint and the ability to degrade many aquatic pollutants, including ECs [8,9]. The fundamental principle of AOPs is the in situ formation of reactive species, such as hydroxyl radicals ($HO^{\bullet}$), which non-selectively attack pollutants, converting them into more biodegradable compounds and ideally mineralizing them [10,11].

Heterogeneous photocatalysis is among the most extensively employed AOPs for the degradation of persistent aquatic pollutants [12,13]. The principal mechanism of photocatalysis involves an electron (e^-_{CB}) being excited from the valence band of a semiconducting material (photocatalyst) to the conduction band upon absorption of a photon whose energy exceeds the material's band gap (E_g) [14,15]. Consequently, this results in the formation of a positive hole in the valence band (h^+_{VB}) [16]. The two photogenerated charges (e^-_{CB}–h^+_{VB} pair) can either recombine or migrate to the surface of the photocatalyst through charge transfer interactions, initiating numerous redox reactions [17]. This process results in the direct transformation and/or degradation of pollutants by e^-_{CB} and h^+_{VB}, or the formation of various reactive species, including $HO^{\bullet}$ and superoxide anion radicals ($O_2^{\bullet -}$), which can also react with adsorbed pollutants [15,18].

According to the existing literature, titanium dioxide (TiO_2) is the most widely employed photocatalyst for wastewater amelioration [19,20]. However, the utilization of TiO_2 under direct solar irradiation is considerably limited by its relatively wide E_g (~3.2 eV), which permits photoactivation solely through ultraviolet (UV) light that constitutes less than 5% of the solar spectrum [21,22]. Therefore, the current scientific trend emphasizes the development of photocatalytic materials capable of utilizing visible-light photons for their activation, harnessing more solar energy [23].

Graphitic carbon nitride (g-C_3N_4) is an emerging n-type polymeric photocatalyst with a relatively narrow E_g (~2.7 eV), enabling its photoactivation under visible light ($\lambda < 460$ nm) [24,25]. The structure of g-C_3N_4 consists of stacked two-dimensional layers of interconnected planar tris-s-triazine (heptazine) units, which are composed of sp^2-hybridized carbon and nitrogen atoms, establishing the π-conjugated electronic structure of the material [26,27]. Generally, it can be synthesized from inexpensive, nitrogen-rich organic precursors such as urea, thiourea, and melamine through the process of thermal polycondensation [28]. Although g-C_3N_4 exhibits attractive features in the field of photocatalysis, such as a narrow E_g, tunable electronic band structure, non-toxicity, thermal and chemical stability, and resistance to photocorrosion, its photocatalytic performance presents some limitations due to the rapid recombination of photogenerated charges [28–30]. To date, numerous strategies have been developed to alter the electronic properties of g-C_3N_4 and suppress the recombination phenomenon. These approaches include doping with alkali metals (e.g., K^+, Na^+, Li^+) [31,32], transition metals (e.g., Fe^{3+}, Ni^{2+}, Cu^{2+}) [33–35], and non-metals (e.g., P, S, B) [36–38], as well as constructing type-II or direct Z-scheme heterojunctions by combining g-C_3N_4 with other semiconductors [18,39,40].

Another interesting approach for improving the photocatalytic performance of g-C_3N_4 is the fabrication of Schottky junctions through the integration of materials exhibiting high metallicity, such as noble metal nanoparticles [41–44]. In this field, 2D MXene materials have been rapidly gaining ground due to their advantageous characteristics. Specifically, their high electrical conductivity (up to 8000 S cm^{-1}), high work function (Φ) that promotes e_{CB}^- migration, and the abundance of surface functional groups (T_x = –O, –OH, –F) that can serve as active sites provide a compelling alternative to costly noble-metal nanoparticles [45–47].

In recent years, some first studies have reported the synthesis of composite photocatalytic materials composed of g-C_3N_4 (prepared from various precursors) and small amounts of $Ti_3C_2T_x$ MXene [48–51]. However, in most cases, g-C_3N_4 was utilized in its

bulk form, which is known to exhibit decreased photocatalytic efficiency compared to its exfoliated counterparts [52–55]. Additionally, the reported composite photocatalysts were primarily used for energy-related applications such as hydrogen production [56,57] or the photocatalytic degradation of dyes (e.g., rhodamine B) [58] and antibiotics (e.g., tetracycline) [48,59]. Therefore, a research gap exists concerning the photocatalytic performance of these materials in degrading other common pharmaceuticals, such as antidepressants and antihypertensive drugs, in aquatic environments.

In this context, g-C_3N_4 was synthesized in the present work through the thermal polycondensation of urea, as numerous reports suggest that urea-derived g-C_3N_4 exhibits superior photocatalytic activity in comparison to those prepared from melamine, thiourea, and dicyandiamide [60–62]. The resultant bulk material was then subjected to three thermal treatment cycles to achieve sufficient exfoliation of the stacked 2D sheets [63]. The choice of thermal exfoliation as the preferred method was based on studies comparing the influence of various exfoliation techniques on the structural characteristics and photocatalytic efficacy of g-C_3N_4 materials. Notably, thermally exfoliated g-C_3N_4 has been reported to exhibit an increased surface area and enhanced photocatalytic performance compared to g-C_3N_4 exfoliated through concentrated acid treatment, liquid ultrasonication, or hydrothermal processing [64,65]. Furthermore, considering that in numerous reports, g-C_3N_4 undergoes protonation to enhance electrostatic attraction with negatively charged MXene particles, a portion of the thermally exfoliated g-C_3N_4 was subjected to hydrochloric acid (HCl) treatment to investigate whether protonation is indeed beneficial [48,66–68]. The synthesis of the composite materials was carried out via simple ultrasonication-assisted mixing under an inert atmosphere [66,69]. The morphological, structural, and optical properties of all synthesized materials were examined using various characterization techniques. Furthermore, their photocatalytic efficacy was evaluated through laboratory-scale experiments, using the antihypertensive drug valsartan (VLS) as a representative EC. The choice of this compound was based on the fact that it is one of the most widely prescribed antihypertensives. As a result, it is frequently detected in WWTP effluents worldwide with concentrations ranging from 534 ng L^{-1} to 11,359 ng L^{-1}, indicating insufficient removal [70–74]. Additionally, previous reports suggest that the presence of VLS in aquatic and soil environments could potentially cause adverse effects on certain native organisms, even at low concentrations [75–77]. To the best of our knowledge, this is the first systematic study comparing protonated and non-protonated, thermally exfoliated g-C_3N_4 in $Ti_3C_2T_x$ MXene-based Schottky junctions. Overall, this research provides insights into the synthesis of exfoliated g-C_3N_4@$Ti_3C_2T_x$ using facile green methods (i.e., thermal exfoliation). It also clarifies whether protonation is a crucial step in the successful fabrication of these materials.

2. Results and Discussion

2.1. Material Characterization

The structural features of all the synthesized photocatalysts were examined using X-ray diffraction (XRD). In Figure 1a, the diffractograms of CNU, CNUex3, and pCNUex3 each display two prominent peaks at approximately 13.1° and 27.3°. The first low-intensity peak is indexed to the (100) lattice plane, which is associated with the in-plane repeating structural packing motif of the heptazine units. Additionally, the second intense peak is ascribed to the (002) lattice plane and corresponds to the stacked graphite-like layers of g-C_3N_4 materials, composed of conjugated aromatic motifs [63,64]. Interestingly, the diffractogram of CNUex3 exhibits an overall reduced intensity compared to that of CNU, indicating increased structural disorder and decreased lateral size of the heptazine layers, which is typical for exfoliated g-C_3N_4 [52,64]. This finding suggests that the thermal exfoliation process was successful. However, in the diffractogram of pCNUex3, the intensity

of the characteristic peak at 27.3° is higher than that of the corresponding peak of CNUex3, likely due to restacking of the g-C_3N_4 nanosheets after acid treatment, which results in increased crystallinity [78].

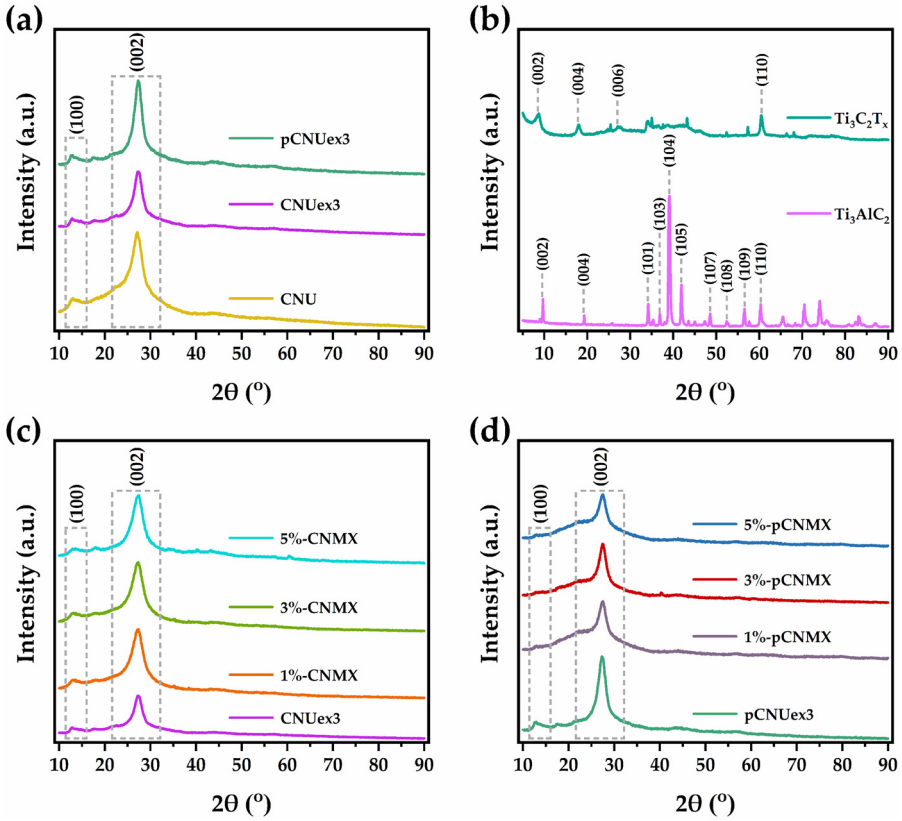


Figure 1. X-ray diffractograms of the synthesized (**a**) CNU, CNUex3, pCNUex3, (**b**) Ti_3AlC_2, $Ti_3C_2T_x$, (**c**) x%-CNMX, and (**d**) x%-pCNMX (x = 1, 3, 5).

The diffractogram of Ti_3AlC_2 (Figure 1b) exhibited sharp, intense peaks centered at 2θ = 9.7°, 19.3°, 34.2°, 36.9°, 39.1°, 41.9°, 48.6°, 52.4°, 56.6°, and 60.3°, which correspond to the (002), (004), (101), (103), (104), (105), (107), (108), (109), and (110) lattice planes. According to previous studies, these peaks are typical of the hexagonal crystalline structure of Ti_3AlC_2 (PDF 00-052-0875) [79,80]. After treating Ti_3AlC_2 with hydrofluoric acid (HF), most of the peaks described above are shifted or absent in the $Ti_3C_2T_x$ diffractogram (Figure 1b). In particular, the absence of the most intense peak at 39.1° (104) is indicative of the successful etching of Al layers (disappearance of non-basal crystal planes), while the slight broadening and shift of the peaks centered at 9.7° (002) and 19.3° (004) (basal crystal planes) to the lower 2θ values of 8.7° and 18.0°, respectively, further confirm the removal of Al, and the addition of surface terminations (e.g., –F and –OH), as well as increased interlayer spacing [81–83]. All these findings align with the results of studies that used similar synthesis protocols for $Ti_3C_2T_x$, indicating its successful formation [46,83,84].

The diffractograms of the x%-CNMX Schottky junctions (Figure 1c) show a slight increase in the peak intensity at 27.3°, possibly due to restacking of the CNUex3 nanosheets during the wet-mixing process. Conversely, for x%-pCNMX materials (Figure 1d), the overall intensity decreases after ultrasonication, likely because of the partial breakdown of the stacked pCNUex3 nanosheets. Apart from these observations, no peaks related to $Ti_3C_2T_x$ can be distinguished in the diffractograms of either x%-CNMX or x%-pCNMX materials, due to their low MXene content. This finding aligns with reports from similar studies [85,86].

The chemical structure and functional groups of the synthesized materials were analyzed using attenuated total reflectance-Fourier transform infrared spectroscopy (ATR-FTIR). According to Figure 2a, CNU, CNUex3, and pCNUex3 exhibit very similar FTIR spectra, with only minor differences. Notably, the sharp band centered at ~ 807 cm^{-1} is associated with the out-of-plane bending vibrations of the tris-s-triazine rings (breathing mode), which constitute the fundamental structural units of g-C_3N_4 materials [87,88]. Additionally, the low-intensity band located at 890 cm^{-1} and the broad band spanning from 3000 to 3450 cm^{-1} are ascribed to the deformation and stretching vibrational modes of the N–H bonds, respectively [52,64]. Both of these bands indicate the presence of uncondensed primary and secondary terminal amino groups in the polymer structure of CNU, CNUex3, and pCNUex3 [88,89]. The bands observed in the region from 1000 to 1700 cm^{-1} are associated with the skeletal stretching of C–N heterocycles (fingerprint region) [90,91]. Specifically, these bands correspond to the stretching vibrations of C–N bonds (1396 and 1452 cm^{-1}) and C=N bonds (1540 and 1627 cm^{-1}) [92,93]. In addition, the bands centered at 1227 and 1312 cm^{-1} are attributed to the stretching vibrations of $(C)_2$–NH (partial condensation) and $(C)_3$–N (complete condensation) units, respectively [94,95]. After thermal exfoliation, the bands at 890 cm^{-1} and 3250 cm^{-1} became more intense, likely due to the breakdown of larger 2D sheets and the formation of additional primary and secondary terminal amino groups. However, the protonation process did not alter the chemical structure of CNUex3, as no new peaks appeared in the FTIR spectrum of pCNUex3, which is virtually identical to that of CNUex3 [49,87].

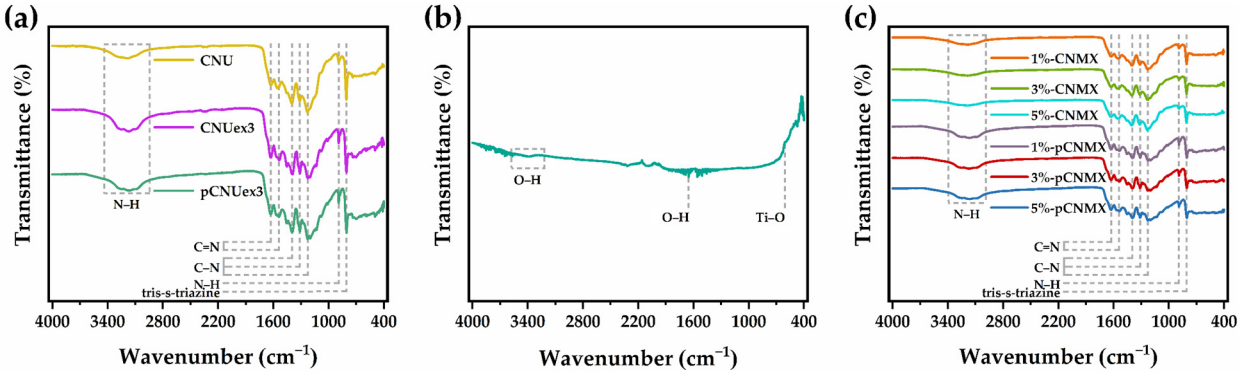


Figure 2. ATR-FTIR spectra of the synthesized (**a**) CNU, CNUex3, pCNUex3, (**b**) $Ti_3C_2T_x$, (**c**) x%-CNMX, and x%-pCNMX (x = 1, 3, 5).

The spectrum of $Ti_3C_2T_x$ (Figure 2b) shows only one prominent band at 631 cm^{-1}, which is ascribed to the deformation vibrations of the Ti–O bond. Closer inspection reveals two additional low-intensity bands at 1653 cm^{-1} and 3300 cm^{-1}, which are attributed to the bending and stretching vibrations of O–H bonds, respectively [96–98]. All these findings suggest that the surface of $Ti_3C_2T_x$ is functionalized with oxygen-containing groups (e.g., –OH) after HF treatment of Ti_3AlC_2.

Interestingly, the FTIR spectra of all synthesized x%-CNMX and x%-pCNMX Schottky junctions (Figure 2c) show an identical profile to that of CNUex3 and pCNUex3, which is expected due to the low $Ti_3C_2T_x$ content in these materials and the extensive coverage of $Ti_3C_2T_x$ particles by exfoliated 2D sheets [49].

Raman spectroscopy measurements were performed to further investigate the structural features of pCNUex3, $Ti_3C_2T_x$, and 1%-pCNMX. According to the Raman spectrum of pCNUex3 (Figure 3a), five Raman bands are identifiable. The most intense band at 706 cm^{-1} and the broad, low-intensity band at 987 cm^{-1} are attributed to different breathing vibrational modes of tris-s-triazine units (A_2' and A_1') [99,100]. Additionally, the bands at 474 cm^{-1} and 752 cm^{-1} are associated with in-plane (twisting) and layer-to-layer vibra-

tions (deformation) of tris-s-triazine rings, respectively [99,100]. Finally, the band centered at 1230 cm^{-1} corresponds to the stretching vibrations of =C (sp^2) atoms [101].

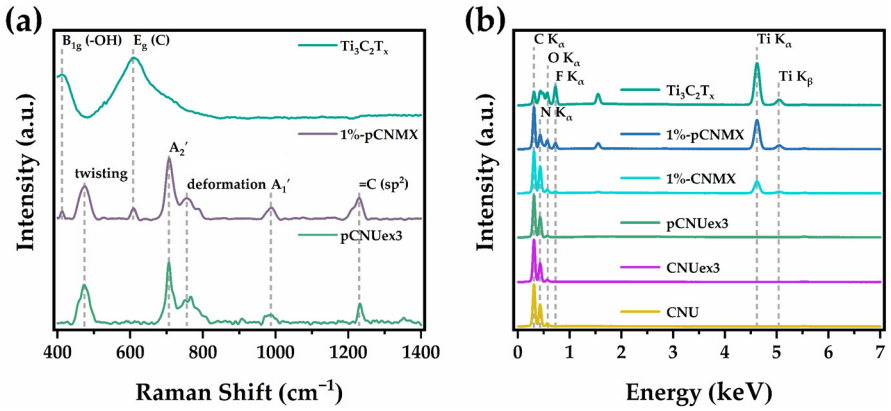


Figure 3. (**a**) Raman spectra of $Ti_3C_2T_x$, pCNUex3, and 1%-pCNMX, as well as (**b**) EDS spectra of CNU, CNUex3, pCNUex3, 1%-CNMX, 1%-pCNMX, and $Ti_3C_2T_x$.

The synthesized MXene displayed two distinct Raman vibrational modes, as depicted in Figure 3a. The less intense band at 412 cm^{-1} corresponds to in-plane stretching vibrations of O (B_{1g}) and indicates –OH terminations, which FTIR also confirmed, while the strongest band at 610 cm^{-1} is attributed to the vibrations of C atoms (E_g) in the $Ti_3C_2T_x$ structure [102,103].

In the case of 1%-pCNMX, all bands related to the vibrational modes of the tris-s-triazine heterocycles are identifiable, along with two low-intensity bands at 412 and 610 cm^{-1}, indicating successful incorporation of the MXene into pCNUex3 sheets.

The energy-dispersive X-ray spectroscopy (EDS) plots for CNU, CNUex3, and pCNUex3 (Figure 3b) display three peaks at 0.30, 0.50, and 0.54 keV, corresponding to the presence of carbon (C K_α), nitrogen (N K_α), and oxygen (O K_α), respectively, on the surfaces of these materials. Therefore, it is apparent that during the thermal polycondensation of urea under a static atmosphere, oxygen-containing groups were introduced onto the surface of CNU. This observation aligns with the EDS findings of other studies that reported the synthesis of g-C_3N_4 materials in the presence of atmospheric air [104,105]. Furthermore, the thermal exfoliation of CNU and the subsequent protonation with HCl did not evidently induce substantial changes in the elemental composition of the material, as indicated in Table S1.

$Ti_3C_2T_x$, as evidenced by its corresponding EDS spectrum (Figure 3b), is composed of titanium (Ti K_α and K_β) and carbon (C K_α), while fluorine (F K_α) and oxygen (O K_α) are present on its surface. This suggests that the preparation protocol of $Ti_3C_2T_x$ led to the incorporation of fluorine and oxygen-containing functionalities on its surface, which is characteristic of MXenes synthesized via wet-chemical etching of MAX phases using HF [106]. Interestingly, the atomic ratio of titanium to carbon is 1.51 (Table S1), indicating that the HF treatment of Ti_3AlC_2 did not compromise the integrity of the titanium and carbon layers. Furthermore, the presence of oxygen confirms the existence of –OH groups, which were identified through ATR-FTIR and Raman spectroscopies.

Analysis of the EDS spectra of the synthesized Schottky junctions indicates that MXene particles were effectively coated by g-C_3N_4 nanosheets, as evidenced by the presence of all characteristic peaks corresponding to the precursors of these materials. However, as indicated in Table S1, 1%-pCNMX appeared to be more extensively covered by g-C_3N_4 nanosheets, given the higher nitrogen content compared to 1%-CNMX. Therefore, protonation seemingly facilitated the attraction between the two materials.

The surface features of CNU, CNUex3, pCNUxe3, 1%-CNMX, and 1%-pCNMX were examined using field-emission scanning electron microscopy (FE-SEM). CNU displayed a sponge-like morphology (Figure 4a) composed of aggregated 2D flakes of varying sizes (< 1 µm), with macro-pores forming among them. After thermal exfoliation (Figure 4b), the flake size is significantly reduced, and the edges of the sheets appear curled, while the material retains its overall fluffy morphology. These observations align with the findings of similar studies where urea-derived g-C_3N_4 was subjected to thermal exfoliation [64,107]. The protonation of CNUex3 results in a more compact structure, as depicted in the FE-SEM micrograph of pCNUex3 (Figure 4c). Specifically, it appears that the nanosheets of CNUex3 aggregated extensively, and the sponge-like structure of the material was significantly diminished. This observation is consistent with the XRD findings, which suggested an increased degree of crystallinity following HCl treatment.

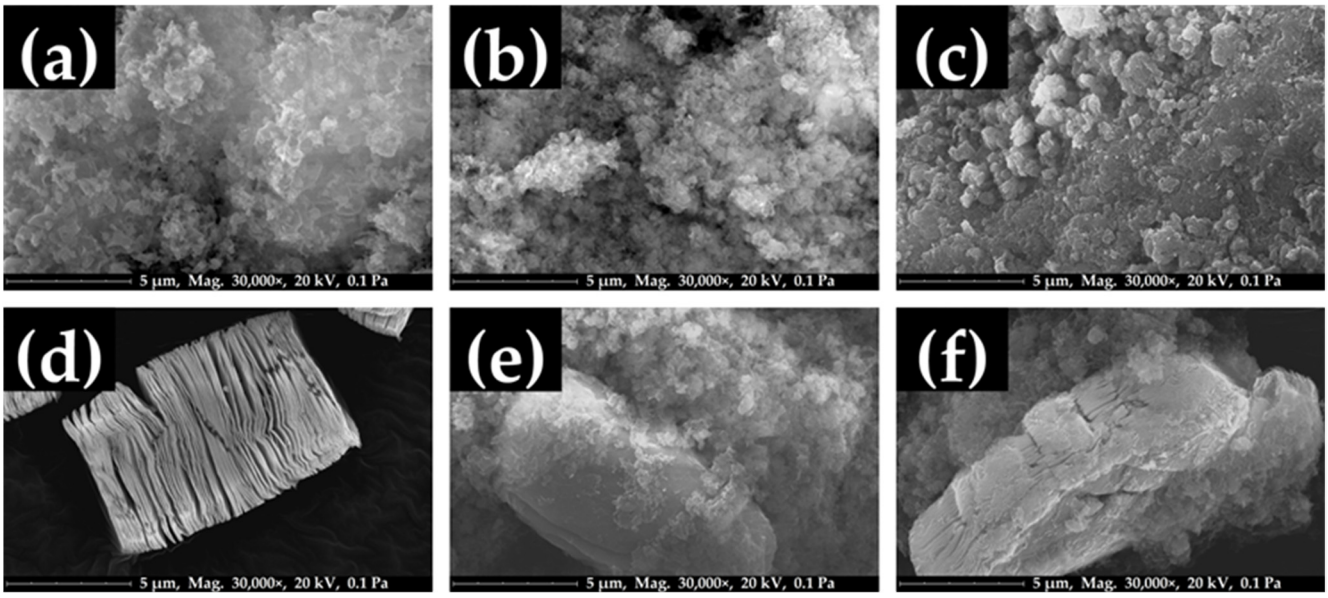


Figure 4. SEM micrographs of (**a**) CNU, (**b**) CNUex3, (**c**) pCNUex3, (**d**) $Ti_3C_2T_x$, (**e**) 1%-CNMX, (**f**) and 1%-pCNMX.

$Ti_3C_2T_x$ exhibits an accordion-like multilayered morphology (Figure 4d), which is primarily ascribed to the wet-chemical etching of Al layers from Ti_3AlC_2. Additionally, it is plausible that the release of hydrogen gases, resulting from the reaction between HF and Al, contributes to this morphological characteristic [83].

The micrograph of 1%-CNMX (Figure 4e) shows that $Ti_3C_2T_x$ particles are incorporated within clusters of CNUex3 nanosheets. Notably, the surface of the MXene is partially coated with CNUex3, while certain regions remain exposed. In the case of 1%-pCNMX, the composite material displays a morphology similar to that of 1%-CNMX (Figure 4f). However, the MXene particles exhibit a higher degree of incorporation within the pCNUex3 cluster owing to the electrostatic attractions between the positively charged nanosheets and the negatively charged MXene. Furthermore, it appears that the ultrasonication process disrupted the compact structure of pCNUex3, resulting in the formation of nanosheets similar to those of CNUex3. This finding is corroborated by the XRD results mentioned earlier.

The EDS elemental maps (Figure 5) further confirm that, in the case of 1%-pCNMX, there is a higher degree of heterocontact between $Ti_3C_2T_x$ and pCNUex3, as the MXene particle is more extensively covered by protonated g-C_3N_4 nanosheets in comparison to 1%-CNMX (non-protonated g-C_3N_4 nanosheets). This observation supports the claim that the electrostatic attraction between $Ti_3C_2T_x$ and pCNUex3 led to the formation of a more uniform material.

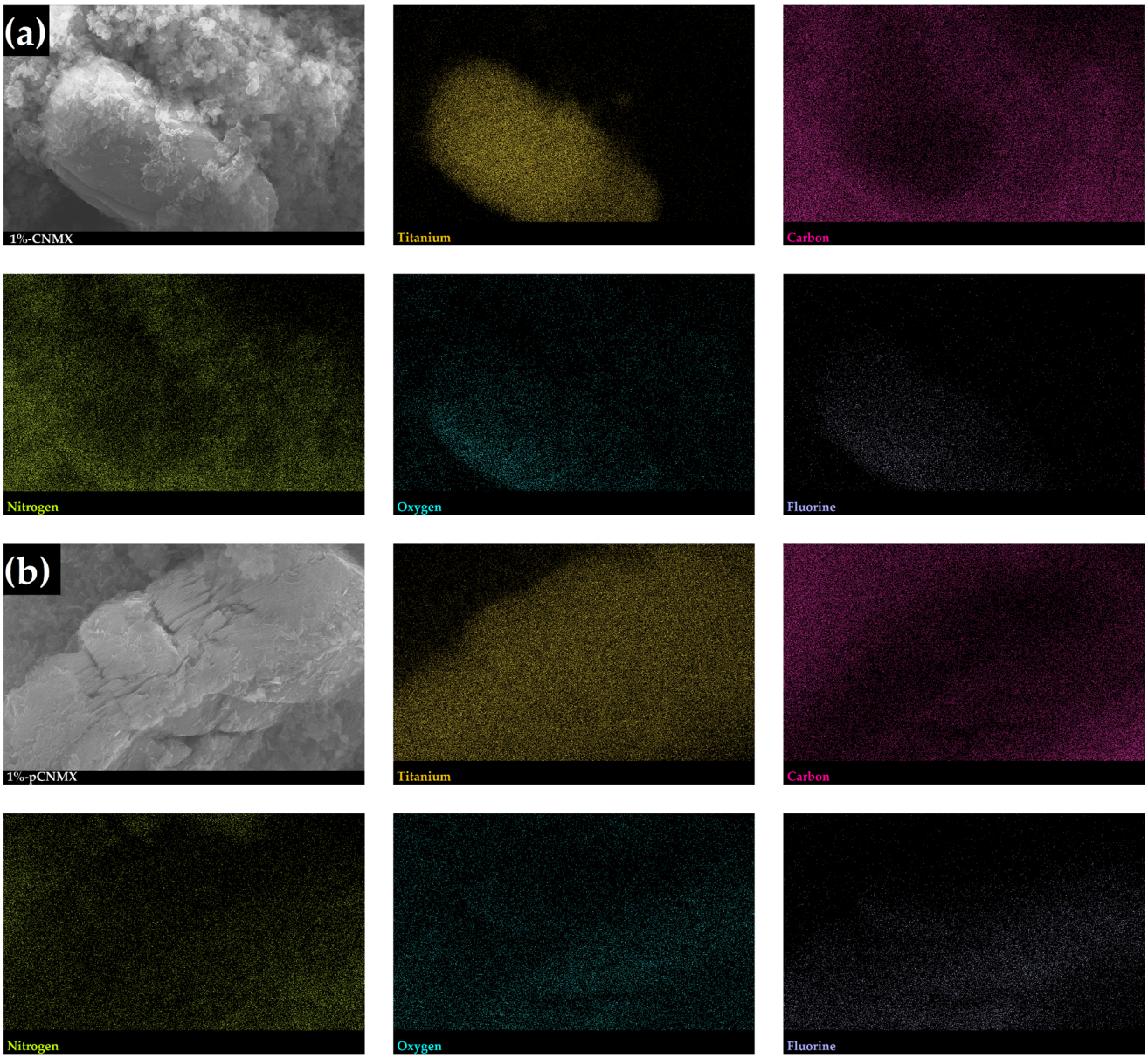


Figure 5. EDS elemental maps of (**a**) 1%-CNMX and (**b**) 1%-pCNMX showing the presence of titanium, carbon, nitrogen, oxygen, and fluorine on the surface of these materials.

The adsorption–desorption isotherms of the synthesized CNU, CNUex3, pCNUex3, 1%-CNMX, and 1%-pCNMX are depicted in Figure 6. All the isotherms are classified as Type IVa, with H3 hysteresis loops, and are typical of mesoporous materials, according to the IUPAC technical report on physisorption. The specific surface area (S_{BET}) of CNU, CNUex3, pCNUex3, 1%-CNMX, and 1%-pCNMX was determined using the Brunauer–Emmett–Teller (BET) equation and measured as 57.2 m^2 g^{-1}, 190.9 m^2 g^{-1}, 117.4 m^2 g^{-1}, 163.1 m^2 $g^{-1,}$ and 121.2 m^2 g^{-1}, respectively. CNU exhibited an S_{BET} that is consistent with reports from similar studies on urea-derived g-C_3N_4 materials [62]. After subjecting CNU to three consecutive thermal treatment cycles, the S_{BET} of the resulting CNUex3 increased by roughly 3.3 times, demonstrating that thermal exfoliation was successful. However, the protonation process had an adverse effect on CNUex3, as evidenced by the substantially lower S_{BET} of pCNUex3. This observation agrees with the results of XRD and SEM analyses. In particular, both methods indicated that pCNUex3 had a denser microstructure compared to CNUex3, which was due to the protonation process that promoted restacking of the g-C_3N_4 nanosheets. In the case of 1%-CNMX, the slight reduction in S_{BET} can be attributed

to the substitution of CNUex3 with MXene, as well as to partial restacking caused by water treatment. Finally, 1%-pCNMX displayed a surface area comparable to that of pCNUex3 despite MXene loading.

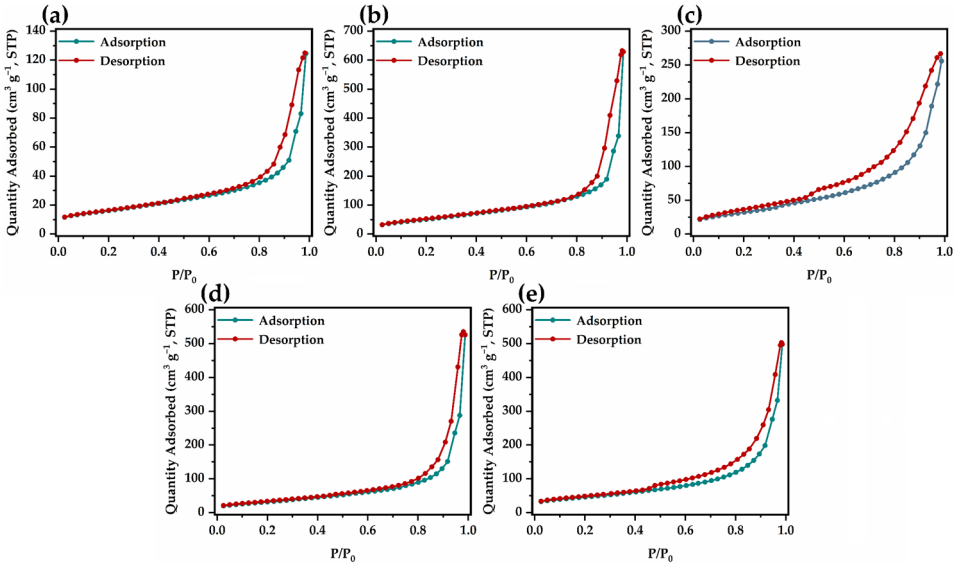


Figure 6. Nitrogen adsorption–desorption isotherms of the synthesized (**a**) CNU, (**b**) CNUex3, (**c**) pCNUex3, (**d**) 1%-CNMX, and (**e**) 1%-pCNMX.

The E_g of the synthesized CNU, CNUex3, pCNUex3, 1%-CNMX, and 1%-pCNUex3 was estimated from the Tauc plots presented in Figure 7 using data obtained from diffuse reflectance spectroscopy (DRS) measurements. CNU has an E_g of 2.85 eV, which is consistent with reports on urea-derived g-C_3N_4 materials [62,108]. After thermal exfoliation, the E_g of the resulting CNUex3 exhibits a slight increase (blue-shift), which could be ascribed to the quantum confinement effect arising from the reduced thickness of the synthesized nanosheets [52,64]. Interestingly, the protonation process did not alter the E_g of CNUex3. However, combining either CNUex3 or pCNUex3 with 1% $Ti_3C_2T_x$ resulted in a slight decrease in the E_g (red-shift), suggesting that the respective Schottky junctions can utilize more visible light photons for photoactivation. This could potentially lead to an increased number of photogenerated e^-_{CB}–h^+_{VB} pairs and, consequently, improved photocatalytic performance.

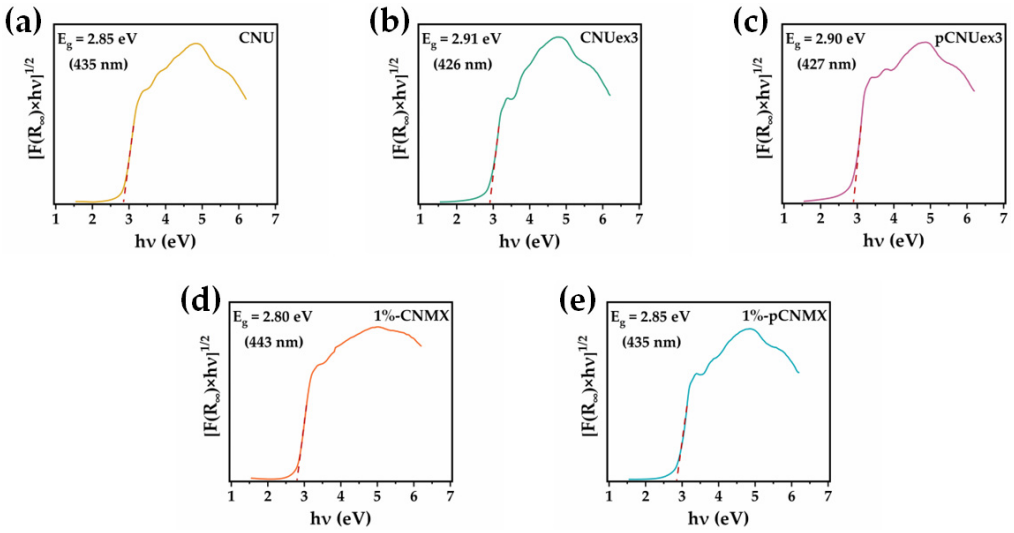


Figure 7. Tauc plots and determined E_g for the synthesized (**a**) CNU, (**b**) CNUex3, (**c**) pCNUex3, (**d**) 1%-CNMX, and (**e**) 1%-pCNMX.

The ability of CNUex3, pCNUex3, and 1%-pCNMX to efficiently separate charge carriers was examined using PL spectroscopy. As shown in Figure 8, pCNUex3 displayed a slightly decreased PL intensity, suggesting that protonation of CNUex3 partially inhibited the recombination of e^-_{CB} and h^+_{VB}. After successfully incorporating $Ti_3C_2T_x$ particles within clusters of pCNUex3 nanosheets, the PL intensity further decreased, indirectly confirming that the 1%-pCNMX Schottky junction was successfully fabricated, as the recombination phenomenon was significantly suppressed [49,109].

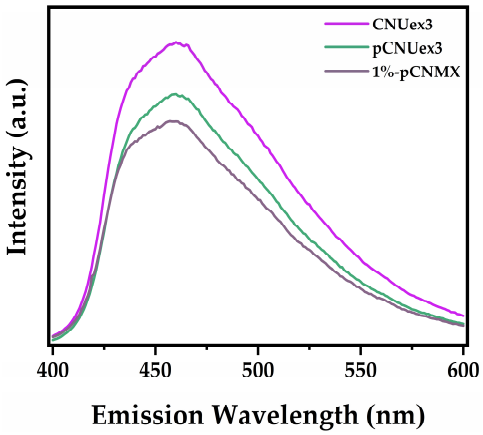


Figure 8. PL spectra of the synthesized CNUex3, pCNUex3, and 1%-pCNMX.

2.2. Photocatalytic Degradation of VLS Using the Synthesized Photocatalysts

The photocatalytic performance of CNUex3, pCNUex3, and the synthesized Schottky junctions x%-CNMX and x%-pCNMX (x = 1, 3, 5) was assessed based on their ability to degrade VLS under simulated solar light. Furthermore, a control experiment (photolysis) was performed in the absence of a photocatalyst to investigate the impact of simulated solar light on the removal of the model pollutant. The degradation kinetics (Figures 9a,b and S1) were fitted to a pseudo-first-order kinetic model, yielding a good correlation ($R^2 > 0.99$), and the resulting kinetic data are presented in Tables 1 and S2. All photocatalytic experiments were conducted in duplicate to evaluate the reproducibility of the synthesized materials, and the relative standard deviation (RSD) in all cases ranged from 0.83% to 8.89% suggesting good reproducibility.

Direct photolysis had minimal impact on VLS degradation, as the initial concentration of the pharmaceutical was reduced by only 7% after 2 h of irradiation. In the presence of CNUex3 and pCNUex3, over 80% of VLS was eliminated within 2 h of irradiation, demonstrating that photocatalysis can effectively remove this frequently detected EC from aqueous environments. In addition, the fact that CNUex3 achieved slightly faster kinetics than pCNUex3 appears to be associated with the increased surface area and, by extension, the increased number of active sites that promote redox reactions. The combination of pCNUex3 with small amounts of $Ti_3C_2T_x$ was indeed beneficial, as 1%-pCNMX and 3%-pCNMX achieved about 47% and 18% faster kinetics, respectively, compared to pCNUex3. However, 5%-pCNMX exhibited a kinetic constant (k_{PC}) comparable to that of pCNUex3, indicating that larger quantities of $Ti_3C_2T_x$ might have the opposite effect owing to the substitution of the photocatalysts by the MXene, which acts as an electron sink. A similar trend was also observed for the x%-CNMX materials, with 1%-CNMX demonstrating the optimum performance, while 3%-CNMX and 5%-CNMX were less efficient even than pCNUex3. The fact that all x%-CNMX materials exhibited slower kinetics than their x%-pCNMX counterparts indicates that protonation is a key step in synthesizing g-C_3N_4@$Ti_3C_2T_x$ Schottky junctions because of the higher incorporation of MXene particles within g-C_3N_4 nanosheets. Considering that the enhanced performance of Schottky

junctions is based on the migration of e^-_{CB} from the conduction band of the photocatalyst to the Fermi level (E_f) of the MXene (Figure 9d), an increased heterocontact between the two materials could, in turn, improve the migration rate [56,110]. Additionally, the built-in electrical field at the interface of pCNUex3 and $Ti_3C_2T_x$ (Schottky barrier) prevents the backflow of e^-_{CB}, thereby suppressing exciton recombination. The importance of hetero-contact between photocatalyst and electro-sink can be further substantiated by the fact that 1%-pCNMX, which has a smaller S_{BET} compared to 1%-CNMX, exhibits, as previously mentioned, faster removal kinetics owing to the better incorporation of MXene particles.

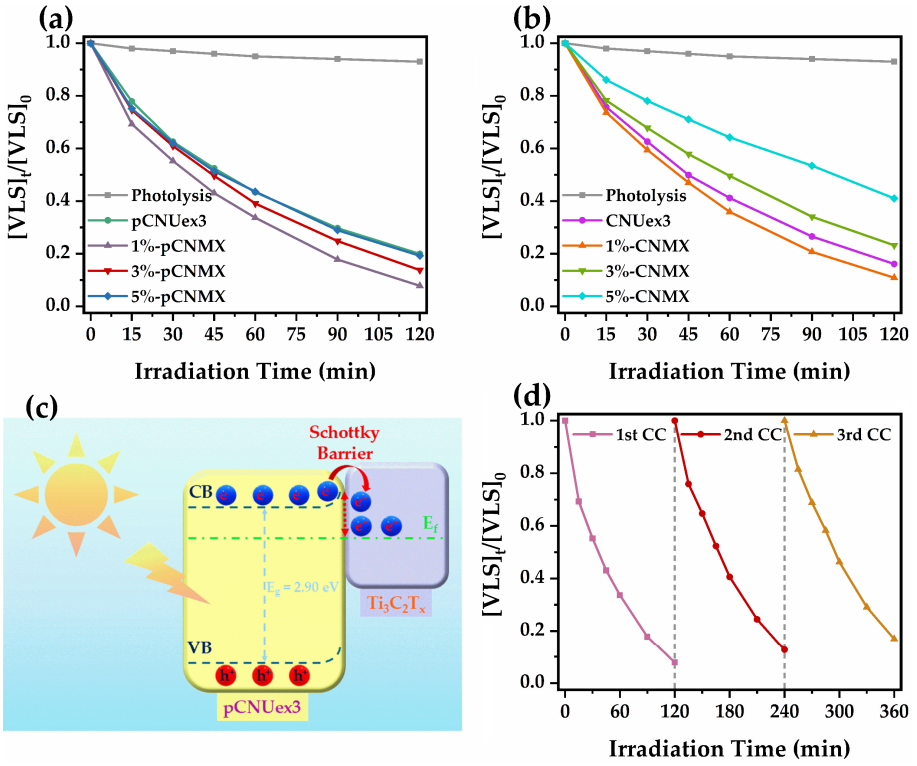


Figure 9. Photocatalytic degradation kinetics of VLS (5 mg L^{-1}) using the synthesized (**a**) CNUex3, x%-CNMX, (**b**) pCNUex3, and x%-pCNMX (100 mg L^{-1}) in the presence of simulated solar light (I = 500 W m^{-2}). (**c**) Schematic representation of the Schottky junction formed between pCNUex3 and $Ti_3C_2T_x$ MXene. (**d**) Photocatalytic degradation cycles of VLS (5 mg L^{-1}) using 1%-pCNMX (100 mg L^{-1}) in the presence of simulated solar light (I = 500 W m^{-2}).

Table 1. Pseudo-first-order photocatalytic degradation constants (k_{PC}), calculated half-lives ($t_{1/2}$), correlation coefficients (R^2), percentage differences of k_{PC} between pCNUex3 and the Schottky junctions (Δk_{PC}), and percentage removals of VLS using the synthesized photocatalysts.

Photocatalyst	k_{PC} (min^{-1})	R^2	$t_{1/2}$ (min)	Removal (%)	Δk_{PC} (%)
None (Photolysis)	0.0007	0.940	990	7.00	-
CNUex3	0.0151	0.998	41.3	83.9	-
pCNUex3	0.0137	0.997	50.6	80.1	-
1%-pCNMX	0.0201	0.993	34.5	92.2	+46.7
3%-pCNMX	0.0161	0.997	43.1	86.2	+17.5
5%-pCNMX	0.0139	0.994	49.9	80.8	+1.46
1%-CNMX	0.0179	0.997	38.7	89.1	+30.7
3%-CNMX	0.0121	0.995	57.3	76.8	−11.7
5%-CNMX	0.0073	0.995	95.0	59.0	−46.7

From a mechanistic perspective, g-C_3N_4-based photocatalysts are extensively studied. According to the existing literature, h^+_{VB} and $O_2^{\bullet-}$ are often recognized as the primary

oxidizing and reducing species, respectively, that facilitate the degradation of various aquatic pollutants [111,112]. Additionally, the generated $HO^{\bullet}$ and $^1O_2$ may also play a role in the degradation mechanism, but to a lesser degree due to their slower production rates [25]. Therefore, in the case of VLS, it could be proposed that when 1%-pCNMX is utilized as a photocatalyst, the degradation is expected to be primarily dominated by $h^+_{VB,}$ which might oxidize the –COOH moiety via the photo-Kolbe mechanism (decarboxylation), or attack electron-rich sites of the compound, such as the tetrazole ring [113,114]. Considering that e^-_{CB} migrate to the E_f of the MXene, more h^+_{VB} are available to react with the adsorbed VLS molecules on the photocatalyst surface, promoting the above-mentioned oxidation reactions.

The stability of 1%-pCNMX, the most efficient among the synthesized Schottky junctions, was evaluated over three consecutive photocatalytic degradation cycles (CCs). As shown in Figure 9d, after the first CC, the photocatalytic performance of 1%-pCNMX declined by 19.4% (Table S3). However, after the second CC, only a 13.5% reduction in kPC was observed. Therefore, the most significant loss in photocatalytic efficiency at the end of the first CC may be linked to the loss of g-C_3N_4 nanosheets during the washing stages, as well as the blocking of several active sites on the photocatalyst surface. Overall, the material demonstrated notable stability, outperforming the unmodified pCNUex3 in photocatalytic performance during the third CC.

3. Materials and Methods

3.1. Reagents, Solvents, and Materials

Urea (99%, ACS reagent) was purchased from Thermo Scientific Chemicals (Waltham, MA, USA). VLS (>98.0%, HPLC) was obtained from Tokyo Chemical Industry (Tokyo, Japan). Titanium aluminum carbide (Ti_3AlC_2) (≥90%, ≤40 μm particle size) and hydrochloric acid (37%, ACS reagent) were supplied by Sigma-Aldrich (St. Louis, MO, USA). HPLC-grade methanol (MeOH), acetonitrile (AcN), absolute ethanol (EtOH), and water were purchased from Fisher Chemical (Pittsburgh, PA, USA). HF (40%, for analysis) and formic acid (FA) (98–100%, for LC-MS) were supplied by Supelco (Bellefonte, PA, USA). All chemicals were used as received without further purification or processing. Ultrapure water (UPW) (0.055 μS cm^{-1}) was acquired on site from an Evoqua water purification system (Pittsburgh, PA, USA).

3.2. Synthesis of Bulk g-C_3N_4

Bulk g-C_3N_4 (CNU) was synthesized from urea following the methodology reported by Papamichail et al., 2023 [62], with minor modifications. In brief, 10 g of urea was ground to a fine powder using an agate mortar and pestle and transferred to a 50 mL alumina crucible. Then, 4.2 mL of UPW was added, and the resulting slurry was magnetically stirred for 15 min and dried at 85 °C for 12 h. Next, the crucible was capped with an alumina lid, and the dried urea slurry was heated to 550 °C for 4 h, under static air with a heating rate of 10 °C min^{-1}. After cooling to room temperature, the pale yellow CNU was collected, thoroughly ground in an agate mortar and pestle, and stored until further use. The synthetic protocol was repeated nine more times, and the average mass yield was 373 mg (3.7%).

3.3. Synthesis of Thermally Exfoliated CNU

Thermally exfoliated CNU (CNUex3) was prepared by subjecting CNU to three consecutive thermal treatment cycles. Specifically, 250 mg of CNU was transferred into a 50 mL alumina crucible, semi-capped with an alumina lid, and heated to 550 °C for 2 h, under static air with a heating rate of 10 °C min^{-1}. The process was repeated two more times, and

after the third cycle, the final pale-yellow material was collected. The synthetic protocol was performed nine additional times, resulting in an average mass yield of 80 mg per 250 mg batch (32%). It should be noted that after each thermal treatment cycle, the mass loss was approximately 33%.

3.4. Synthesis of Protonated CNUex3 (pCNUex3)

Protonated CNUex3 (pCNUex3) was prepared through acid treatment. Briefly, 400 mg of CNUex3 was dispersed in 40 mL of aqueous HCl (0.5 M) with magnetic stirring for 15 min. The dispersion was then bath-sonicated for 1 h, with the bath temperature maintained at 25 °C using ice. Next, the sonicated suspension was magnetically stirred for an additional 4 h at room temperature, followed by centrifugation for 15 min at 4500 rpm. The supernatant was decanted, and the precipitate was washed with 30 mL of ultrapure water (UPW) in repeated vortexing–centrifugation cycles until the supernatant pH reached 4.5. Finally, the precipitate was collected and dried at 80 °C for 12 h. After cooling to room temperature, pCNUex3 was ground with an agate mortar and pestle and stored until further use. The yield of the protonation process was 360 mg (90%).

3.5. Synthesis of $Ti_3C_2T_x$ MXene

$Ti_3C_2T_x$ MXene was synthesized through wet-chemical etching of the Al layer in Ti_3AlC_2 MAX phase. First, 20 mL of 40% HF was transferred into a PTFE round-bottom flask. 1 g of Ti_3AlC_2 was then slowly added (at 100 mg min^{-1}) while stirring to minimize violent bubbling and heating, which occur due to the exothermic reaction between HF and Al. The flask was then immersed in a silicon-oil bath thermostated at 60 °C, and a PTFE condenser was mounted on top of it. Water circulation was initiated and maintained throughout the synthesis process to limit HF loss, while allowing hydrogen gases generated during the reaction to vent safely into a fume hood. After stirring for 24 h at 60°C, the suspension was centrifuged for 15 min at 4500 rpm. The supernatant was decanted, and the precipitate was repeatedly washed with 40 mL of UPW (vortexing–centrifugation cycles) until the supernatant pH reached 6. The precipitated $Ti_3C_2T_x$ MXene was then washed three times with EtOH and dried at 60°C under a continuous nitrogen flow (50 L h^{-1}) for 8 h. Finally, the dried $Ti_3C_2T_x$ was collected and stored at 4°C in the dark until further use. The mass yield of $Ti_3C_2T_x$ was 384 mg (38.4%). It is important to note that, due to HF's highly toxic nature, safety procedures outlined by Shuck et al. (2021) were followed throughout all stages of the synthesis [115].

3.6. Synthesis of x%-CNMX and x%-pCNMX Schottky Junctions

x%-CNMX and x%-pCNMX (x = 1, 3, 5) Schottky junctions were fabricated using a facile ultrasonication-assisted mixing method similar to that described in the literature [50,69]. First, 95, 97, or 99 mg of pCNUex3 (or CNUex3) was dispersed in 30 mL of UPW with magnetic stirring for 15 min. The suspension was then subjected to ultrasonication (45 kHz) for 2 h, utilizing a Hielscher UP100H ultrasonication probe (Berlin, Germany). Afterward, 5, 3, or 1 mg of $Ti_3C_2T_x$ MXene was added, and ultrasonication continued for 2 h. Throughout the synthesis process, the suspension was immersed in a water bath maintained at 25 °C to prevent overheating from ultrasonication and was purged with nitrogen to avoid oxidation of the MXene. The resulting materials were centrifuged at 4500 rpm for 10 min and dried at 60°C under a continuous nitrogen flow (50 L h^{-1}) for 8 h. Finally, they were ground with an agate mortar and pestle and stored at 4 °C in the dark until further use. The mass yield of x%-CNMX and x%-pCNMX was practically 100%. The "x" denotes the mass percent of $Ti_3C_2T_x$ MXene in each of the synthesized Schottky junctions.

3.7. Material Characterization Techniques

3.7.1. XRD Analysis

X-ray diffractograms of CNU, CNUex3, pCNUex3, and the synthesized Schottky junctions were recorded using a Bruker D8 Advance diffractometer (Billerica, MA, USA) with monochromatic Cu-K_α radiation (λ = 1.5406 Å). Diffractograms were acquired over 2θ = 10 to 90° with the scan rate set at 0.1° min^{-1}.

3.7.2. ATR-FTIR Spectroscopy

ATR-FTIR spectra of CNU, CNUex3, pCNUex3, and the synthesized Schottky junctions were recorded in the range of 400–4000 cm^{-1} with a resolution of 2 cm^{-1} using a Shimadzu IRSpirit spectrometer (Kyoto, Japan) equipped with a QATR-S attachment. A total of 45 scans were collected and averaged per spectrum.

3.7.3. Raman Spectroscopy

Raman spectra of pCNUex3, $Ti_3C_2T_x$ MXene, and 1%-pCNMX were obtained using a Horiba Scientific LabRAM Soleil confocal laser Raman microscope (Lyon, France). Sample excitation was performed with a 785 nm laser, and spectra were recorded within the Raman shift range of 100–1700 cm^{-1}. The number of accumulations was set to 3 with an acquisition time of 20 sec each. Baseline correction for each sample was carried out using HORIBA's LabSpec 6 software (Lyon, France).

3.7.4. FE-SEM and EDS Analysis

FE-SEM micrographs of CNU, CNUex3, pCNUex3, $Ti_3C_2T_x$ MXene, 1%-CNMX, and 1%-pCNMX were acquired using a Thermo Fisher Pharos Phenom G2 FEG-SEM (Waltham, MA, USA) operated at 0.1 Pa (high-vacuum mode) with an electron beam accelerating voltage of 20 kV. Before imaging, all samples were sputter-coated with a 5 nm layer of chromium using a Quantum Design Plus sputter coater (Darmstadt, Germany) to enhance surface conductivity and image quality.

EDS spectra of the photocatalysts were recorded during SEM imaging under the same operational conditions (0.1 Pa, 20 kV) at a magnification of 20,000× using the aforementioned FE-SEM microscope, which is equipped with an EDS detector. Three distinct regions of each selected sample were analyzed, and the atomic concentrations presented in Table S1 are the average values of these analyses.

3.7.5. Nitrogen Porosimetry Measurements

Adsorption–desorption isotherms of CNU, CNUex3, pCNUex3, 1%-pCNMX, and 1%-CNMX were obtained at 77 K (liquid nitrogen temperature) utilizing a Quantachrome Autosorb iQ porosimeter (Bounton Beach, FL, USA). Before analysis, approximately 100 mg of each photocatalyst was transferred into a 9 mm measuring glass cell and degassed under vacuum at 150 °C overnight. Afterwards, the corresponding rod was inserted into the glass cell, and measurement was initiated. The S_{BET} of the photocatalysts was calculated using the BET equation within a relative pressure range of 0.05 to 0.30 [116].

3.7.6. DRS Measurements

DRS measurements of CNU, CNUex3, pCNUex3, and the synthesized Schottky junctions were performed using a Shimadzu UV-2600 spectrophotometer (Kyoto, Japan) equipped with an ISR-2600Plus integrating sphere. Spectra were recorded in the UV–Vis range (200–800 nm) with a scan interval of 0.5 nm, using barium sulfate ($BaSO_4$) as a reference material.

The E_g of the photocatalysts mentioned above was estimated by converting their reflectance spectra into absorption spectra using the Tauc equation, where the absorption

coefficient (α) was replaced by the Kubelka-Munk function ($F(R_\infty)$) [117]. Considering that g-C_3N_4 is an indirect E_g semiconductor, the exponent γ was set to 2 in all cases [118]. $[F(R_\infty) \times h\nu]^{1/2}$ was then plotted against hν, and E_g was identified as the point where the tangent line to the linear region intersected the x-axis [117,119].

3.7.7. PL Spectroscopy

PL spectra of CNUex3, pCNUex3, and 1%-pCNMX were obtained using a Horiba FluoroMax-4 spectrofluorometer (Lyon, France). The photocatalysts were excited with 320 nm monochromatic radiation, and emission spectra were recorded from 400–600 nm with a 1 nm step.

3.8. Laboratory-Scale Photocatalytic Experiments

Laboratory-scale photocatalytic experiments were conducted using an Atlas Suntest XLS+ solar light simulator (Linsengericht, Germany) equipped with a 2.2 kW Xenon lamp covered by a cut-off filter (λ > 290 nm). Initially, a double-walled Pyrex reactor was positioned on top of a magnetic stirrer at the center of the reflective irradiation chamber and maintained at 25 ± 2 °C by continuous water circulation. Next, a 100 mL solution of VLS (5 mg L^{-1}), prepared with UPW (pH ~ 7), was transferred into the reactor, and a 5 mL aliquot of the reactor contents was collected using an automatic pipette (t = −30 min). Subsequently, 9.5 mg of photocatalyst (100 mg L^{-1}) was added, and the suspension was magnetically stirred (200 rpm) in the dark for 30 min to reach adsorption–desorption equilibrium. Another sample of the reactor content was taken after the adsorption (t = 0 min), and the irradiation process was started. The simulated solar radiation intensity (I) was set to 500 W m^{-2} and maintained throughout the photocatalytic process. During the experiment, 5 mL samples were collected after specific irradiation time periods (15, 30, 45, 60, 90, and 120 min). Each sample was filtered through a hydrophobic PTFE syringe filter (0.22 μm pore size) to remove suspended photocatalyst and stored in glass vials at 4°C in the dark until further analysis.

For the reusability experiments, the same protocol was employed, with the sole modification being that during the initial CC, the volume of the aqueous VLS solution was 300 mL to facilitate the recovery of the photocatalyst. At the end of each CC, the residual 1%-pCNMX was recovered through centrifugation at 4500 rpm for 10 min. Subsequently, the precipitated photocatalyst was washed three times with UPW and MeOH via centrifugation-redispersion cycles and then dried under a nitrogen flow at 80 °C for 6 h. The dried photocatalyst was collected, weighed, and used in the next CC, after adjusting the initial volume of the aqueous VLS solution accordingly to maintain a photocatalyst dose of 100 mg L^{-1}.

3.9. Determination of VLS Concentration in Photocatalysis Samples

The residual concentration of VLS in the samples collected during the photocatalytic experiments was measured via high-performance liquid chromatography with photodiode array detection (HPLC-PDA). The analysis was conducted on a Shimadzu Nexera HPLC system, consisting of an SPD-M40 photodiode array detector, an LC-40D solvent delivery pump, and a CTO-40C column oven. Chromatographic separation of the analytes was achieved with a Supelco Discovery HS C18 column (250 mm × 4.6 mm, 5 μm particle size) (Bellefonte, PA, USA). Isocratic elution was carried out with a mobile phase consisting of MeOH, AcN, and water + 0.1% $^{V}/_{V}$ FA (20:40:40) at a flow rate of 1 mL min^{-1}. The column temperature was maintained at 40 °C, and the injection volume was 20 μL. VLS detection was performed at λ_{max} = 203 ± 4 nm, with a retention time of 8.4 min. A seven-point calibration curve within the concentration range of 0.1 to 5 mg L^{-1} ($R^2 > 0.999$) was used to quantify VLS (LOQ = 0.066 mg L^{-1}, LOD = 0.021 mg L^{-1}).

4. Conclusions

The present study reports the facile synthesis of thermally exfoliated g-C_3N_4@$Ti_3C_2T_x$ MXene Schottky junctions using an ultrasonication-assisted wet mixing protocol. Additionally, it systematically examines how protonation of the exfoliated g-C_3N_4 precursor affects the uniformity of the fabricated composite materials and, by extension, their photocatalytic performance. According to the kinetic results of photocatalytic experiments with VLS (model EC), the optimal MXene amount for either CNUex3 or pCNUex3 is 1% by weight. Notably, the protonated variants show higher photocatalytic efficiency than their non-protonated versions. This observation indicates that an increased level of heterocontact between the positively charged surface of pCNUex3 and the negatively charged surface of $Ti_3C_2T_x$ was accomplished, promoting charge migration and consequently limiting photogenerated charge recombination. In light of this, it appears that incorporating exfoliated MXene materials or MXene quantum dots into protonated g-C_3N_4-based photocatalysts in future research may lead to improved photocatalytic performance due to the enhanced dispersibility of these materials and, by extension, their potential for increased heterocontact. Furthermore, the protonation of g-C_3N_4 can enable the one-step electrostatic synthesis of ternary heterojunctions that include another photocatalyst with a negative zeta potential (such as WO_3) and MXene, thus facilitating the development of Z-scheme/Schottky systems that are expected to exhibit significantly improved photocatalytic efficiency. Overall, this work strongly indicates that protonation of g-C_3N_4 is crucial for synthesizing MXene-based Schottky junctions, which remain highly promising in the field of environmental photocatalysis for pollutant removal and green fuel production.

Supplementary Materials: The following supporting information can be downloaded at: https://www.mdpi.com/article/10.3390/catal15090909/s1, Figure S1: Logarithmic photocatalytic degradation kinetics of VLS (5 mg L^{-1}) using the synthesized (a) CNUex3, x%-CNMX, (b) pCNUex3, and x%-pCNMX (100 mg L^{-1}) in the presence of simulated solar light (I = 500 W m^{-2}). Table S1: Elemental composition of $Ti_3C_2T_x$, CNU, CNUex3, pCNUex3, 1%-CNMX, and 1%-pCNMX, as determined by EDS elemental analysis and atomic ratios of carbon to nitrogen (C:N). Table S2: Pseudo-first order photocatalytic degradation constants (k_{PC}) and correlation coefficients (R^2) of the logarithmic degradation kinetics of VLS. Table S3: Pseudo-first order photocatalytic degradation constants (k_{PC}), calculated half-lives ($t_{1/2}$), correlation coefficients (R^2), percentage difference of k_{PC} between each CC (Δk_{PC}), and percentage removals of VLS using 1%-pCNMX for each CC.

Author Contributions: Conceptualization, I.K.; methodology, I.K.; formal analysis, C.L.; investigation, C.L.; resources, I.K.; data curation, C.L.; writing—original draft preparation, C.L.; writing—review and editing, I.K.; visualization, C.L.; supervision, I.K.; project administration, I.K.; funding acquisition, I.K. All authors have read and agreed to the published version of the manuscript.

Funding: This research was funded by the project "Advanced Nanostructured Materials for Sustainable Growth: Green Energy Production/Storage, Energy Saving and Environmental Remediation" (TAEDR-0535821), which is implemented under the action "Flagship actions in interdisciplinary scientific fields with a special focus on the productive fabric" (ID 16618), Greece 2.0—National Recovery and Resilience Fund, and funded by European Union NextGenerationEU.

Data Availability Statement: Data are contained within the article.

Conflicts of Interest: The authors declare no conflicts of interest.

References

1. Intisar, A.; Ramzan, A.; Hafeez, S.; Hussain, N.; Irfan, M.; Shakeel, N.; Gill, K.A.; Iqbal, A.; Janczarek, M.; Jesionowski, T. Adsorptive and Photocatalytic Degradation Potential of Porous Polymeric Materials for Removal of Pesticides, Pharmaceuticals, and Dyes-Based Emerging Contaminants from Water. *Chemosphere* **2023**, *336*, 139203. [CrossRef] [PubMed]
2. Simonovic, S.P. World Water Dynamics: Global Modeling of Water Resources. *J. Environ. Manag.* **2002**, *66*, 249–267. [CrossRef]

3. Kumar, R.; Qureshi, M.; Vishwakarma, D.K.; Al-Ansari, N.; Kuriqi, A.; Elbeltagi, A.; Saraswat, A. A Review on Emerging Water Contaminants and the Application of Sustainable Removal Technologies. *Case Stud. Chem. Environ. Eng.* **2022**, *6*, 100219. [CrossRef]
4. Nishmitha, P.S.; Akhilghosh, K.A.; Aiswriya, V.P.; Ramesh, A.; Muthuchamy, M.; Muthukumar, A. Understanding emerging contaminants in water and wastewater: A comprehensive review on detection, impacts, and solutions. *J. Hazard. Mater. Adv.* **2025**, *18*, 100755. [CrossRef]
5. Jelic, A.; Gros, M.; Ginebreda, A.; Cespedes-Sánchez, R.; Ventura, F.; Petrovic, M.; Barcelo, D. Occurrence, Partition and Removal of Pharmaceuticals in Sewage Water and Sludge during Wastewater Treatment. *Water Res.* **2011**, *45*, 1165–1176. [CrossRef] [PubMed]
6. Liu, S.-S.; You, W.-D.; Chen, C.-E.; Wang, X.-Y.; Yang, B.; Ying, G.-G. Occurrence, Fate and Ecological Risks of 90 Typical Emerging Contaminants in Full-Scale Textile Wastewater Treatment Plants from a Large Industrial Park in Guangxi, Southwest China. *J. Hazard. Mater.* **2023**, *449*, 131048. [CrossRef]
7. Salimi, M.; Esrafili, A.; Gholami, M.; Jafari, A.J.; Kalantary, R.R.; Farzadkia, M.; Kermani, M.; Sobhi, H.R. Contaminants of Emerging Concern: A Review of New Approach in AOP Technologies. *Environ. Monit. Assess.* **2017**, *189*, 414. [CrossRef]
8. Lykos, C.; Kourkouta, T.; Konstantinou, I. Study on the photocatalytic degradation of metronidazole antibiotic in aqueous media with TiO_2 under lab and pilot scale. *Sci. Total. Environ.* **2023**, *870*, 161877. [CrossRef]
9. Zawadzki, P. Visible Light–Driven Advanced Oxidation Processes to Remove Emerging Contaminants from Water and Wastewater: A Review. *Water Air Soil Pollut.* **2022**, *233*, 374. [CrossRef]
10. Fast, S.A.; Gude, V.G.; Truax, D.D.; Martin, J.; Magbanua, B.S. A Critical Evaluation of Advanced Oxidation Processes for Emerging Contaminants Removal. *Environ. Process.* **2017**, *4*, 283–302. [CrossRef]
11. Antonopoulou, A.; Konstantinou, I. Photocatalytic degradation and mineralization of tramadol pharmaceutical in aqueous TiO_2 suspensions: Evaluation of kinetics, mechanisms and ecotoxicity. *Appl. Catal. A Gen.* **2016**, *515*, 136–143. [CrossRef]
12. Garrido-Cardenas, J.A.; Esteban-García, B.; Agüera, A.; Sánchez-Pérez, J.A.; Manzano-Agugliaro, F. Wastewater Treatment by Advanced Oxidation Process and Their Worldwide Research Trends. *Int. J. Environ. Res. Public Health* **2019**, *17*, 170. [CrossRef]
13. Rapti, I.; Kosma, C.; Albanis, T.; Konstantinou, I. Solar Photocatalytic Degradation of Inherent Pharmaceutical Residues in Real Hospital WWTP Effluents Using Titanium Dioxide on a CPC Pilot Scale Reactor. *Catal Today* **2022**, *423*, 113884. [CrossRef]
14. Rauf, M.A.; Ashraf, S.S. Fundamental principles and application of heterogeneous photocatalytic degradation of dyes in solution. *Chem. Eng. J.* **2009**, *151*, 10–18. [CrossRef]
15. Zhang, Y.; Zhou, B.; Chen, H.; Yuan, R. Heterogeneous photocatalytic oxidation for the removal of organophosphorus pollutants from aqueous solutions: A review. *Sci. Total. Environ.* **2022**, *856*, 159048. [CrossRef] [PubMed]
16. Su, R.; Zhu, Y.; Gao, B.; Li, Q. Progress on Mechanism and Efficacy of Heterogeneous Photocatalysis Coupled Oxidant Activation as an Advanced Oxidation Process for Water Decontamination. *Water Res.* **2024**, *251*, 121119. [CrossRef]
17. Morshedy, A.S.; El-Fawal, E.M.; Zaki, T.; El-Zahhar, A.A.; Alghamdi, M.M.; El Naggar, A.M.A. A review on heterogeneous photocatalytic materials: Mechanism, perspectives, and environmental and energy sustainability applications. *Inorg. Chem. Commun.* **2024**, *163*, 112307. [CrossRef]
18. Lykos, C.; Bairamis, F.; Efthymiou, C.; Konstantinou, I. Synthesis and Characterization of Composite WO_3 Fibers/g-C_3N_4 Photocatalysts for the Removal of the Insecticide Clothianidin in Aquatic Media. *Nanomaterials* **2024**, *14*, 1045. [CrossRef] [PubMed]
19. Mukherjee, J.; Lodh, B.K.; Sharma, R.; Mahata, N.; Shah, M.P.; Mandal, S.; Ghanta, S.; Bhunia, B. Advanced oxidation process for the treatment of industrial wastewater: A review on strategies, mechanisms, bottlenecks and prospects. *Chemosphere* **2023**, *345*, 140473. [CrossRef]
20. Zhang, Y.; Hawboldt, K.; Zhang, L.; Lu, J.; Chang, L.; Dwyer, A. Carbonaceous Nanomaterial-TiO_2 Heterojunctions for Visible-Light-Driven Photocatalytic Degradation of Aqueous Organic Pollutants. *Appl. Catal. A Gen.* **2022**, *630*, 118460. [CrossRef]
21. John, A.; Rajan, M.S.; Thomas, J. Carbon Nitride-Based Photocatalysts for the Mitigation of Water Pollution Engendered by Pharmaceutical Compounds. *Environ. Sci. Pollut. Res.* **2021**, *28*, 24992–25013. [CrossRef] [PubMed]
22. Dong, S.; Feng, J.; Fan, M.; Pi, Y.; Hu, L.; Han, X.; Liu, M.; Sun, J.; Sun, J. Recent Developments in Heteroge-neous Photocatalytic Water Treatment Using Visible Light-Responsive Photocatalysts: A Review. *RSC Adv.* **2015**, *5*, 14610–14630. [CrossRef]
23. Lee, D.-E.; Kim, M.-K.; Danish, M.; Jo, W.-K. State-of-the-art review on photocatalysis for efficient wastewater treatment: Attractive approach in photocatalyst design and parameters affecting the photocatalytic degradation. *Catal. Commun.* **2023**, *183*, 106764. [CrossRef]
24. Alaghmandfard, A.; Ghandi, K. A Comprehensive Review of Graphitic Carbon Nitride (g-C_3N_4)–Metal Oxide-Based Nanocomposites: Potential for Photocatalysis and Sensing. *Nanomaterials* **2022**, *12*, 294. [CrossRef]
25. Lykos, C.; Sioulas, S.; Konstantinou, I. g-C_3N_4 as Photocatalyst for the Removal of Metronidazole Antibiotic from Aqueous Matrices under Lab and Pilot Scale Conditions. *Catalysts* **2023**, *13*, 254. [CrossRef]

26. Inagaki, M.; Tsumura, T.; Kinumoto, T.; Toyoda, M. Graphitic Carbon Nitrides (g-C_3N_4) with Comparative Discussion to Carbon Materials. *Carbon* **2019**, *141*, 580–607. [CrossRef]
27. Bhanderi, D.; Lakhani, P.; Modi, C.K. Graphitic Carbon Nitride (g-C_3N_4) as an Emerging Photocatalyst for Sustainable Environmental Applications: A Comprehensive Review. *RSC Sustain.* **2023**, *2*, 265–287. [CrossRef]
28. Bairamis, F.; Rapti, I.; Konstantinou, I. g-C_3N_4 Based Z-Scheme Photocatalysts for Environmental Pollutants Removal. *Curr. Opin. Green Sustain. Chem.* **2022**, *40*, 100749. [CrossRef]
29. Khan, M.A.; Mutahir, S.; Shaheen, I.; Qunhui, Y.; Bououdina, M.; Humayun, M. Recent Advances over the Doped g-C_3N_4 in Photocatalysis: A Review. *Co-ord. Chem. Rev.* **2024**, *522*, 216227. [CrossRef]
30. Luo, Y.; Wei, X.; Gao, B.; Zou, W.; Zheng, Y.; Yang, Y.; Zhang, Y.; Tong, Q.; Dong, L. Synergistic adsorption-photocatalysis processes of graphitic carbon nitrate (g-C_3N_4) for contaminant removal: Kinetics, models, and mechanisms. *Chem. Eng. J.* **2019**, *375*, 122019. [CrossRef]
31. Jiang, J.; Cao, S.; Hu, C.; Chen, C. A comparison study of alkali metal-doped g-C_3N_4 for visible-light photocatalytic hydrogen evolution. *Chin. J. Catal.* **2017**, *38*, 1981–1989. [CrossRef]
32. Yan, W.; Yan, L.; Jing, C. Impact of Doped Metals on Urea-Derived g-C_3N_4 for Photocatalytic Degradation of Antibiotics: Structure, Photoactivity and Degradation Mechanisms. *Appl. Catal. B Environ.* **2019**, *244*, 475–485. [CrossRef]
33. Ma, T.; Shen, Q.; Zhaoa, J.X.B.; Guan, R.; Liu, X.; Jia, H.; Xu, B. Facile Synthesis of Fe-Doped g-C_3N_4 for Enhanced Visible-Light Photocatalytic Activity. *Inorg. Chem. Commun.* **2019**, *107*, 107451. [CrossRef]
34. Bao, J.; Bai, W.; Wu, M.; Gong, W.; Yu, Y.; Zheng, K.; Liu, L. Template-Mediated Copper Doped Porous g-C_3N_4 for Efficient Photodegradation of Antibiotic Contaminants. *Chemosphere* **2022**, *293*, 133607. [CrossRef] [PubMed]
35. Meng, X.; Wang, M.; Hu, J.; Liu, Q.; Tang, H. The Synergistic Effect of P Doping and Ni(II) Electron Cocatalyst Boosting Photocatalytic H_2-Evolution Activity of g-C_3N_4. *Ceram. Int.* **2021**, *47*, 23386–23395. [CrossRef]
36. Liu, S.; Zhu, H.; Yao, W.; Chen, K.; Chen, D. One Step Synthesis of P-Doped g-C_3N_4 with the Enhanced Visible Light Photocatalytic Activity. *Appl. Surf. Sci.* **2018**, *430*, 309–315. [CrossRef]
37. Chen, P.; Xing, P.; Chen, Z.; Lin, H.; He, Y. Rapid and Energy-Efficient Preparation of Boron Doped g-C_3N_4 with Excellent Performance in Photocatalytic H_2-Evolution. *Int. J. Hydrogen Energy* **2018**, *43*, 19984–19989. [CrossRef]
38. Ge, L.; Han, C.; Xiao, X.; Guo, L.; Li, Y. Enhanced visible light photocatalytic hydrogen evolution of sulfur-doped polymeric g-C_3N_4 photocatalysts. *Mater. Res. Bull.* **2013**, *48*, 3919–3925. [CrossRef]
39. Rapti, I.; Bairamis, F.; Konstantinou, I. g-C_3N_4/MoS_2 Heterojunction for Photocatalytic Removal of Phenol and Cr(VI). *Photochem* **2021**, *1*, 358–370. [CrossRef]
40. Obregón, S.; Ruíz-Gómez, M.A.; Rodríguez-González, V.; Vázquez, A.; Hernández-Uresti, D.B. A Novel Type-II $Bi_2W_2O_9$/g-C_3N_4 Heterojunction with Enhanced Photocatalytic Performance under Simulated Solar Irradiation. *Mater. Sci. Semicond. Process.* **2020**, *113*, 105056. [CrossRef]
41. Zhang, X.; Yang, P. Advances in Noble Metal-Modified g-C_3N_4 Heterostructures toward Enhanced Photocatalytic Redox Ability. *Int. J. Miner. Metall. Mater.* **2024**, *31*, 2368–2389. [CrossRef]
42. Nie, L.; Chen, H.; Wang, J.; Yang, Y.; Fang, C. Enhanced Visible-Light H_2O_2 Production over Pt/g-C_3N_4 Schottky Junction Photocatalyst. *Inorg. Chem.* **2024**, *63*, 4770–4782. [CrossRef]
43. Saman, F.; Bahruji, H.; Mahadi, A.H.; Ling, C.H.S. Pd/g-C_3N_4 Photocatalyst for Hydrogen Production: Role of Experimental Condition for Schottky Barrier. *Fuel* **2023**, *349*, 128725. [CrossRef]
44. Wang, H.; Sun, T.; Chang, L.; Nie, P.; Zhang, X.; Zhao, C.; Xue, X. The g-C_3N_4 Nanosheets Decorated by Plasmonic Au Nanoparticles: A Heterogeneous Electrocatalyst for Oxygen Evolution Reaction Enhanced by Sunlight Illumination. *Electrochimica Acta* **2019**, *303*, 110–117. [CrossRef]
45. Jin, Y.; Geng, J.; Wang, J.; Ren, F.; Chen, Z.; Sun, Z.; Yan, C.; Ren, P.-G. Recent advances of MXenes in the photocatalytic pollutant degradations for environmental applications: A mini review. *J. Environ. Chem. Eng.* **2023**, *11*, 110052. [CrossRef]
46. Pang, X.; Xue, S.; Zhou, T.; Qiao, M.; Li, H.; Liu, X.; Xu, Q.; Liu, G.; Lei, W. Noble Metal-Free Heterojunction of Ultrathin Ti_3C_2 MXene/WO_3 for Boosted Visible-Light-Driven Photoreactivity. *Adv. Sustain. Syst.* **2022**, *7*, 2100507. [CrossRef]
47. Sherryna, A.; Tahir, M. Role of Ti_3C_2MXene as Prominent Schottky Barriers in Driving Hydrogen Production through Photoinduced Water Splitting: A Comprehensive Review. *ACS Appl. Energy Mater.* **2021**, *4*, 11982–12006. [CrossRef]
48. Li, C.; Kan, C.; Meng, X.; Liu, M.; Shang, Q.; Yang, Y.; Wang, Y.; Cui, X. Self-Assembly 2D Ti_3C_2/g-C_3N_4 MXene Heterojunction for Highly Efficient Photocatalytic Degradation of Tetracycline in Visible Wavelength Range. *Nanomaterials* **2022**, *12*, 4015. [CrossRef]
49. Xu, H.; Xiao, R.; Huang, J.; Jiang, Y.; Zhao, C.; Yang, X. In Situ Construction of Protonated g-C_3N_4/Ti_3C_2 MXene Schottky Heterojunctions for Efficient Photocatalytic Hydrogen Production. *Chin. J. Catal.* **2021**, *42*, 107–114. [CrossRef]
50. Liu, W.; Sun, M.; Ding, Z.; Gao, B.; Ding, W. Ti_3C_2 MXene Embellished g-C_3N_4 Nanosheets for Improving Photocatalytic Redox Capacity. *J. Alloys Compd.* **2021**, *877*, 160223. [CrossRef]
51. Li, J.; Zhang, Q.; Zou, Y.; Cao, Y.; Cui, W.; Dong, F.; Zhou, Y. Ti_3C_2 MXene Modified g-C_3N_4 with Enhanced Visible-Light Photocatalytic Performance for NO Purification. *J. Colloid Interface Sci.* **2020**, *575*, 443–451. [CrossRef]

52. Papailias, I.; Todorova, N.; Giannakopoulou, T.; Ioannidis, N.; Boukos, N.; Athanasekou, C.P.; Dimotikali, D.; Trapalis, C. Chemical vs Thermal Exfoliation of g-C_3N_4 for NO_x Removal under Visible Light Irradiation. *Appl. Catal. B Environ.* **2018**, *239*, 16–26. [CrossRef]
53. Pattnaik, S.P.; Behera, A.; Martha, S.; Acharya, R.; Parida, K. Facile Synthesis of Exfoliated Graphitic Carbon Nitride for Photocatalytic Degradation of Ciprofloxacin under Solar Irradiation. *J. Mater. Sci.* **2019**, *54*, 5726–5742. [CrossRef]
54. Antonopoulou, M.; Bika, P.; Papailias, I.; Zervou, S.-K.; Vrettou, A.; Efthimiou, I.; Mitrikas, G.; Ioannidis, N.; Trapalis, C.; Dallas, P.; et al. Photocatalytic Degradation of Organic Micropollutants under UV-A and Visible Light Irradiation by Exfoliated g-C_3N_4 Catalysts. *Sci. Total. Environ.* **2023**, *892*, 164218. [CrossRef]
55. Qiu, P.; Chen, H.; Xu, C.; Zhou, N.; Jiang, F.; Wang, X.; Fu, Y. Fabrication of an Exfoliated Graphitic Carbon Nitride as a Highly Active Visible Light Photocatalyst. *J. Mater. Chem. A* **2015**, *3*, 24237–24244. [CrossRef]
56. Lee, D.-E.; Jyothirmai, M.V.; Mameda, N.; Jo, W.-K.; Tonda, S. 2D/2D Schottky-Type Hybrid Heterocatalyst Comprising S-Doped g-C_3N_4 and Delaminated Ti_3C_2 MXene: Synergistic Interplay of Dual Strategies for Effective H_2 Generation and Pollutant Degradation. *Appl. Surf. Sci.* **2024**, *669*, 160516. [CrossRef]
57. Husain, A.; Lee, D.-E.; Siddiqui, Q.T.; Gunnasegaran, P.; Danish, M.; Jo, W.-K. Scalable Integration of MOFs, COFs, and MXenes with g-C_3N_4 for Solar H_2 Generation: A Review of Energy Conversion Strategies. *Int. J. Hydrogen Energy* **2025**, *150*, 150041. [CrossRef]
58. Huang, K.; Li, C.; Wang, L.; Wang, W.; Meng, X. Layered Ti_3C_2 MXene and Silver Co-Modified g-C_3N_4 with Enhanced Visible Light-Driven Photocatalytic Activity. *Chem. Eng. J.* **2021**, *425*, 131493. [CrossRef]
59. Dong, H.; Zhang, X.; Zuo, Y.; Song, N.; Xin, X.; Zheng, B.; Sun, J.; Chen, G.; Li, C. 2D Ti_3C_2 as Electron Harvester Anchors on 2D g-C_3N_4 to Create Boundary Edge Active Sites for Boosting Photocatalytic Performance. *Appl. Catal. A Gen.* **2020**, *590*, 117367. [CrossRef]
60. Li, K.; Chen, M.; Chen, L.; Zhao, S.; Xue, W.; Han, Z.; Han, Y. Synthesis of g-C_3N_4 Derived from Different Precursors for Photodegradation of Sulfamethazine under Visible Light. *Processes* **2023**, *11*, 528. [CrossRef]
61. Xia, P.; Li, G.; Li, X.; Yuan, S.; Wang, K.; Huang, D.; Ji, Y.; Dong, Y.; Wu, X.; Zhu, L.; et al. Synthesis of g-C_3N_4 from Various Precursors for Photocatalytic H_2 Evolution under the Visible Light. *Crystals* **2022**, *12*, 1719. [CrossRef]
62. Papamichail, P.; Nannou, C.; Giannakoudakis, D.A.; Bikiaris, N.D.; Papoulia, C.; Pavlidou, E.; Lambropoulou, D.; Samanidou, V.; Deliyanni, E. Maximization of the photocatalytic degradation of diclofenac using polymeric g-C_3N_4 by tuning the precursor and the synthetic protocol. *Catal. Today* **2023**, *418*, 114075. [CrossRef]
63. Todorova, N.; Papailias, I.; Giannakopoulou, T.; Ioannidis, N.; Boukos, N.; Dallas, P.; Edelmannová, M.; Reli, M.; Kočí, K.; Trapalis, C. Photocatalytic H_2 Evolution, CO_2 Reduction, and NO_x Oxidation by Highly Exfoliated g-C_3N_4. *Catalysts* **2020**, *10*, 1147. [CrossRef]
64. Zhang, M.; Yang, Y.; An, X.; Zhao, J.; Bao, Y.; Hou, L.-A. Exfoliation method matters: The microstructure-dependent photoactivity of g-C_3N_4 nanosheets for water purification. *J. Hazard. Mater.* **2022**, *424*, 127424. [CrossRef] [PubMed]
65. Huang, J.; Klahn, M.; Tian, X.; Dai, X.; Rabeah, J.; Aladin, V.; Corzilius, B.; Bartling, S.; Lund, H.; Steinfeldt, N.; et al. Exfoliated Polymeric Carbon Nitride Nanosheets for Photocatalytic Applications. *Acs Appl. Nano Mater.* **2024**, *7*, 7442–7452. [CrossRef]
66. Yang, Y.; Zeng, Z.; Zeng, G.; Huang, D.; Xiao, R.; Zhang, C.; Zhou, C.; Xiong, W.; Wang, W.; Cheng, M.; et al. Ti_3C_2 Mxene/porous g-C_3N_4 interfacial Schottky junction for boosting spatial charge separation in photocatalytic H_2O_2 production. *Appl. Catal. B Environ.* **2019**, *258*, 117956. [CrossRef]
67. Hu, J.; Ding, J.; Zhong, Q. Ultrathin 2D Ti3C2 MXene Co-Catalyst Anchored on Porous g-C_3N_4 for Enhanced Photocatalytic CO_2 Reduction under Visible-Light Irradiation. *J. Colloid Interface Sci.* **2021**, *582*, 647–657. [CrossRef]
68. Liu, D.; Li, C.; Ge, J.; Zhao, C.; Zhao, Q.; Zhang, F.; Ni, T.; Wu, W. 3D interconnected g-C_3N_4 hybridized with 2D Ti_3C_2 MXene nanosheets for enhancing visible light photocatalytic hydrogen evolution and dye contaminant elimination. *Appl. Surf. Sci.* **2022**, *579*, 152180. [CrossRef]
69. Lou, C.-W.; Xie, M.-M.; Yang, Y.-D.; Wang, H.-Y.; Wang, Z.-K.; Zhang, L.; Hsieh, C.-T.; Liu, L.-Y.; Lin, M.-C.; Li, T.-T. Carbon Nanofiber Membranes Loaded with MXene@g-C_3N_4: Preparation and Photocatalytic Property. *Nanomaterials* **2024**, *14*, 896. [CrossRef]
70. Anagnostopoulou, K.; Evgenidou, E.; Alampanos, V.; Lambropoulou, D.A. High-resolution mass spectrometry approaches for screening persistent and Mobile organic compounds in wastewaters: Target analysis, suspect analysis and risk assessment. *Sci. Total. Environ.* **2025**, *967*, 178777. [CrossRef]
71. Proctor, K.; Altamirano, J.; Kasprzyk-Hordern, B. Chemicals of Emerging Concern in Wastewater Treatment Plants from Mendoza: Environmental Study in a Semiarid Region of Argentina. *J. Hazard. Mater. Adv.* **2025**, *18*, 100662. [CrossRef]
72. Yao, L.; Hu, Y.; Yang, J.-H.; Wu, R.; Chen, F.-L.; Zhou, X. Wastewater Surveillance for Chronic Disease Drugs in Wastewater Treatment Plants: Mass Load, Removal, and Sewage Epidemiology. *J. Hazard. Mater.* **2025**, *489*, 137661. [CrossRef] [PubMed]

73. Lopez-Herguedas, N.; Irazola, M.; Alvarez-Mora, I.; Orive, G.; Lertxundi, U.; Olivares, M.; Zuloaga, O.; Prieto, A. Comprehensive Micropollutant Characterization of Wastewater during Covid-19 Crisis in 2020: Suspect Screening and Environmental Risk Prioritization Strategy. *Sci. Total. Environ.* **2023**, *873*, 162281. [CrossRef]
74. Ofrydopoulou, A.; Nannou, C.; Evgenidou, E.; Christodoulou, A.; Lambropoulou, D. Assessment of a wide array of organic micropollutants of emerging concern in wastewater treatment plants in Greece: Occurrence, removals, mass loading and potential risks. *Sci. Total. Environ.* **2022**, *802*, 149860. [CrossRef]
75. Mezzelani, M.; Peruzza, L.; D'ERrico, G.; Milan, M.; Gorbi, S.; Regoli, F. Mixtures of environmental pharmaceuticals in marine organisms: Mechanistic evidence of carbamazepine and valsartan effects on Mytilus galloprovincialis. *Sci. Total. Environ.* **2022**, *860*, 160465. [CrossRef]
76. Medici, A.; Lavorgna, M.; Isidori, M.; Russo, C.; Orlo, E.; Luongo, G.; Di Fabio, G.; Zarrelli, A. Advanced oxidation process of valsartan by activated peroxymonosulfate: Chemical characterization and ecotoxicological effects of its byproducts. *Sci. Total. Environ.* **2023**, *908*, 168337. [CrossRef] [PubMed]
77. Gallego, S.; Nos, D.; Montemurro, N.; Sanchez-Hernandez, J.C.; Pérez, S.; Solé, M.; Martin-Laurent, F. Ecotoxicological impact of the antihypertensive valsartan on earthworms, extracellular enzymes and soil bacterial communities. *Environ. Pollut.* **2021**, *275*, 116647. [CrossRef]
78. Zheng, C.-J.; Zhang, R.-C.; Xu, K.; Zhang, J.; Wang, K.; Chen, W.; Huang, G.-B.; Yin, H. Protonated g-C_3N_4/Oxygen-Doped g-C_3N_4 S-Scheme Homojunction Fabricated by Electrostatic Self-Assembly for Photocatalytic Hydrogen Evolution and Tetracycline Hydrochloride Degradation. *Carbon* **2024**, *226*, 119153. [CrossRef]
79. Naguib, M.; Kurtoglu, M.; Presser, V.; Lu, J.; Niu, J.; Heon, M.; Hultman, L.; Gogotsi, Y.; Barsoum, M.W. Two-Dimensional Nanocrystals Produced by Exfoliation of Ti_3AlC_2. *Adv. Mater.* **2011**, *23*, 4248–4253. [CrossRef]
80. Cai, T.; Wang, L.; Liu, Y.; Zhang, S.; Dong, W.; Chen, H.; Yi, X.; Yuan, J.; Xia, X.; Liu, C.; et al. Ag_3PO_4/Ti_3C_2 MXene interface materials as a Schottky catalyst with enhanced photocatalytic activities and anti-photocorrosion performance. *Appl. Catal. B Environ.* **2018**, *239*, 545–554. [CrossRef]
81. Kumar, G.; Ahlawat, A.; Bhardwaj, H.; Sahu, G.K.; Rana, P.S.; Solanki, P.R. Ultrasonication-Assisted Synthesis of Transition Metal Carbide of MXene: An Efficient and Promising Material for Photocatalytic Organic Dyes Degradation of Rhodamine B and Methylene Blue in Wastewater. *Environ. Sci. Pollut. Res.* **2024**, *31*, 38232–38250. [CrossRef]
82. Zhong, R.; Liang, Y.; Huang, F.; Liang, S.; Liu, S. Regulating interfacial coupling of 1D crystalline g-C_3N_4 nanorods with 2D $Ti_3C_2T_x$ MXene for boosting photocatalytic CO_2 reduction. *Chin. J. Catal.* **2023**, *53*, 109–122. [CrossRef]
83. Alhabeb, M.; Maleski, K.; Anasori, B.; Lelyukh, P.; Clark, L.; Sin, S.; Gogotsi, Y. Guidelines for Synthesis and Processing of Two-Dimensional Titanium Carbide ($Ti_3C_2T_x$ MXene). *Chem. Mater.* **2017**, *29*, 7633–7644. [CrossRef]
84. Sun, B.; Qiu, P.; Liang, Z.; Xue, Y.; Zhang, X.; Yang, L.; Cui, H.; Tian, J. The fabrication of 1D/2D CdS nanorod@Ti_3C_2 MXene composites for good photocatalytic activity of hydrogen generation and ammonia synthesis. *Chem. Eng. J.* **2021**, *406*, 127177. [CrossRef]
85. Wong, K.J.; Foo, J.J.; Siang, T.J.; Khoo, V.; Ong, W. Harnessing the Power of Light: The Synergistic Effects of Crystalline Carbon Nitride and $Ti_3C_2T_x$ MXene in Photocatalytic Hydrogen Production. *Glob. Chall.* **2024**, *8*, 2300235. [CrossRef]
86. Jin, D.; Lv, Y.; He, D.; Zhang, D.; Liu, Y.; Zhang, T.; Cheng, F.; Zhang, Y.-N.; Sun, J.; Qu, J. Photocatalytic Degradation of COVID-19 Related Drug Arbidol Hydrochloride by Ti_3C_2 MXene/Supramolecular g-C_3N_4 Schottky Junction Photocatalyst. *Chemosphere* **2022**, *308*, 136461. [CrossRef] [PubMed]
87. Ong, W.-J.; Tan, L.-L.; Chai, S.-P.; Yong, S.-T.; Mohamed, A.R. Surface charge modification via protonation of graphitic carbon nitride (g-C_3N_4) for electrostatic self-assembly construction of 2D/2D reduced graphene oxide (rGO)/g-C_3N_4 nanostructures toward enhanced photocatalytic reduction of carbon dioxide to methane. *Nano Energy* **2015**, *13*, 757–770. [CrossRef]
88. Zhu, B.; Xia, P.; Ho, W.; Yu, J. Isoelectric Point and Adsorption Activity of Porous g-C_3N_4. *Appl. Surf. Sci.* **2015**, *344*, 188–195. [CrossRef]
89. Karami, P.; Khani, R. Potential of cobalt ferrite-graphitic carbon nitride nanocomposite in trace determination of pyrene as one of the priority pollutants in water and food samples. *Spectrochim. Acta Part A Mol. Biomol. Spectrosc.* **2023**, *301*, 122969. [CrossRef]
90. Cao, Y.; Li, Q.; Wang, W. Construction of a Crossed-Layer-Structure MoS_2/g-C_3N_4 Heterojunction with Enhanced Photocatalytic Performance. *RSC Adv.* **2017**, *7*, 6131–6139. [CrossRef]
91. Schwinghammer, K.; Mesch, M.B.; Duppel, V.; Ziegler, C.; Senker, J.; Lotsch, B.V. Crystalline Carbon Nitride Nanosheets for Improved Visible-Light Hydrogen Evolution. *J. Am. Chem. Soc.* **2014**, *136*, 1730–1733. [CrossRef]
92. Narkbuakaew, T.; Sujaridworakun, P. Synthesis of Tri-S-Triazine Based g-C_3N_4 Photocatalyst for Cationic Rhodamine B Degradation under Visible Light. *Top. Catal.* **2020**, *63*, 1086–1096. [CrossRef]
93. Liu, H.; Chen, D.; Wang, Z.; Jing, H.; Zhang, R. Microwave-assisted molten-salt rapid synthesis of isotype triazine-/heptazine based g-C_3N_4 heterojunctions with highly enhanced photocatalytic hydrogen evolution performance. *Appl. Catal. B Environ.* **2017**, *203*, 300–313. [CrossRef]

94. Roshni, C.P.; Jithesh, K.; Manuraj, M.; Raj, K.G.; Rakhi, R.B. β-$Ni(OH)_2$ supported over g-C_3N_4: A novel catalyst for para-nitrophenol reduction and supercapacitor electrode. *Results Chem.* **2022**, *4*, 100498. [CrossRef]
95. Al Mamari, S.; Thangavel, S.; Kim, Y.; Selvaraj, R. Enhanced photocatalytic activity of-Fe_2O_3/g-C_3N_4 composite materials for degradation of toluene in aqueous solution under visible light irradiation. *Desalination Water Treat.* **2022**, *254*, 94–103. [CrossRef]
96. Alkhudaydi, A.M.; Danish, E.Y.; Lima, E.C.; Gabal, M.A.; Abdel Salam, M. Photocatalytic Degradation of Malachite Green Dye Using Ti_3C_2 MXene Nanosheets Decorated with Fe_3O_4 NPs under Visible Light Irradiation. *Res. Chem. Intermed.* **2024**, *50*, 5117–5135. [CrossRef]
97. Kiran, N.U.; Deore, A.B.; More, M.A.; Late, D.J.; Rout, C.S.; Mane, P.; Chakraborty, B.; Besra, L.; Chatterjee, S. Comparative Study of Cold Electron Emission from 2D $Ti_3C_2T_X$ MXene Nanosheets with Respect to Its Pre-cursor Ti_3SiC_2 MAX Phase. *Acs Appl. Electron. Mater.* **2022**, *4*, 2656–2666. [CrossRef]
98. Mahmood, M.; Rasheed, A.; Ayman, I.; Rasheed, T.; Munir, S.; Ajmal, S.; Agboola, P.O.; Warsi, M.F.; Shahid, M. Synthesis of Ultrathin MnO_2 nanowire-Intercalated 2D-MXenes for High-Performance Hybrid Supercapacitors. *Energy Fuels* **2021**, *35*, 3469–3478. [CrossRef]
99. Abid, M.Z.; Tanveer, A.; Rafiq, K.; Rauf, A.; Jin, R.; Hussain, E. Proceeding of Catalytic Water Splitting on Cu/Ce@g-C_3N_4 Photocatalysts: An Exceptional Approach for Sunlight-Driven Hydrogen Generation. *Nanoscale* **2024**, *16*, 7154–7166. [CrossRef]
100. Zhou, J.; Zha, X.; Chen, Z.; Li, K.; Sun, H.; Wang, J.; Lv, K.; Cong, S.; Zhao, Z. Tailoring the coordination microenvironment of single-atom W for efficient photocatalytic CO_2 reduction. *Appl. Catal. B Environ.* **2024**, *350*, 123911. [CrossRef]
101. Jiménez-Calvo, P.; Marchal, C.; Cottineau, T.; Caps, V.; Keller, V. Influence of the Gas Atmosphere during the Synthesis of g-C_3N_4 for Enhanced Photocatalytic H_2 Production from Water on Au/g-C_3N_4 Composites. *J. Mater. Chem. A* **2019**, *7*, 14849–14863. [CrossRef]
102. Li, J.; Chen, S.; Ai, Z.; Zhao, X.; Li, Z.; Tian, L.; Yang, Z.; Liang, H. Solvothermal Synthesis of $CdTiO_3$/Ti_3C_2 MXene Composite as a New Efficient Visible Light Photocatalyst. *Colloids Surf. A Physicochem. Eng. Asp.* **2024**, *702*, 134936. [CrossRef]
103. Dixit, P.; Maiti, T. A Facile Pot Synthesis of (Ti_3AlC_2) MAX Phase and Its Derived MXene ($Ti_3C_2T_x$). *Ceram. Int.* **2022**, *48*, 36156–36165. [CrossRef]
104. Fan, J.; Qin, H.; Jiang, S. Mn-Doped g-C_3N_4 Composite to Activate Peroxymonosulfate for Acetaminophen Degradation: The Role of Superoxide Anion and Singlet Oxygen. *Chem. Eng. J.* **2019**, *359*, 723–732. [CrossRef]
105. Shahabi, S.S.; Azizi, N.; Vatanpour, V.; Yousefimehr, N. Novel Functionalized Graphitic Carbon Nitride Incorporated Thin Film Nanocomposite Membranes for High-Performance Reverse Osmosis Desalination. *Sep. Purif. Technol.* **2020**, *235*, 116134. [CrossRef]
106. Zadegan, M.S.J.; Moosaei, R.; Choopani, L.; Salehi, M.M.; Maleki, A.; Zare, E.N. Remediation of Safranin-O and acid fuchsin by using Ti_3C_2 MXene/rGO-Cu_2O nanocomposite: Preparation, characterization, isotherm, kinetic and thermodynamic studies. *Environ. Res.* **2024**, *258*, 119469. [CrossRef]
107. Jiang, X.; Li, X.; Liu, Y.; Zhai, H.; Wang, G. The Oxidative Thermal Exfoliation-Dependent Microstructure and Photocatalytic Performance of g-C_3N_4 Nanosheets. *Diam. Relat. Mater.* **2024**, *143*, 110918. [CrossRef]
108. Pérez-Molina, L.; Pastrana-Martínez, L.M.; Morales-Torres, S.; Maldonado-Hódar, F.J. Photodegradation of Cytostatic Drugs by g-C_3N_4: Synthesis, Properties and Performance Fitted by Selecting the Appropriate Precursor. *Catal. Today* **2023**, *418*, 114068. [CrossRef]
109. Li, J.; Zhao, L.; Wang, S.; Li, J.; Wang, G.; Wang, J. In situ fabrication of 2D/3D g-C_3N_4/Ti_3C_2 (MXene) heterojunction for efficient visible-light photocatalytic hydrogen evolution. *Appl. Surf. Sci.* **2020**, *515*, 145922. [CrossRef]
110. Liu, N.; Lu, N.; Su, Y.; Wang, P.; Quan, X. Fabrication of g-C_3N_4/Ti_3C_2 composite and its visible-light photocatalytic capability for ciprofloxacin degradation. *Sep. Purif. Technol.* **2019**, *211*, 782–789. [CrossRef]
111. Zheng, Q.; Xu, E.; Park, E.; Chen, H.; Shuai, D. Looking at the Overlooked Hole Oxidation: Photocatalytic Transformation of Organic Contaminants on Graphitic Carbon Nitride under Visible Light Irradiation. *Appl. Catal. B Environ.* **2019**, *240*, 262–269. [CrossRef]
112. Zheng, Q.; Durkin, D.P.; Elenewski, J.E.; Sun, Y.; Banek, N.A.; Hua, L.; Chen, H.; Wagner, M.J.; Zhang, W.; Shuai, D. Visible-Light-Responsive Graphitic Carbon Nitride: Rational Design and Photocatalytic Applications for Water Treatment. *Environ. Sci. Technol.* **2016**, *50*, 12938–12948. [CrossRef]
113. Bairamis, F.; Konstantinou, I. Photocatalytic Degradation Pathways of the Valsartan Drug by TiO_2 and g-C_3N_4 Catalysts. *Reactions* **2022**, *3*, 160–171. [CrossRef]
114. Park, H.; Kim, H.-I.; Moon, G.-H.; Choi, W. Photoinduced Charge Transfer Processes in Solar Photocatalysis Based on Modified TiO_2. *Energy Environ. Sci.* **2015**, *9*, 411–433. [CrossRef]
115. Shuck, C.E.; Ventura-Martinez, K.; Goad, A.; Uzun, S.; Shekhirev, M.; Gogotsi, Y. Safe Synthesis of MAX and MXene: Guidelines to Reduce Risk during Synthesis. *Acs Chem. Heal. Saf.* **2021**, *28*, 326–338. [CrossRef]

116. Thommes, M.; Kaneko, K.; Neimark, A.V.; Olivier, J.P.; Rodriguez-Reinoso, F.; Rouquerol, J.; Sing, K.S.W. Physisorption of Gases, with Special Reference to the Evaluation of Surface Area and Pore Size Distribution (IUPAC Technical Report). *Pure Appl. Chem.* **2015**, *87*, 1051–1069. [CrossRef]
117. Makuła, P.; Pacia, M.; Macyk, W. How To Correctly Determine the Band Gap Energy of Modified Semiconductor Photocatalysts Based on UV-Vis Spectra. *J. Phys. Chem. Lett.* **2018**, *9*, 6814–6817. [CrossRef]
118. Liu, J. Effect of phosphorus doping on electronic structure and photocatalytic performance of g-C_3N_4: Insights from hybrid density functional calculation. *J. Alloys Compd.* **2016**, *672*, 271–276. [CrossRef]
119. Landi, S.; Segundo, I.R.; Freitas, E.; Vasilevskiy, M.; Carneiro, J.; Tavares, C.J. Use and misuse of the Kubelka-Munk function to obtain the band gap energy from diffuse reflectance measurements. *Solid State Commun.* **2022**, *341*, 114573. [CrossRef]

Disclaimer/Publisher's Note: The statements, opinions and data contained in all publications are solely those of the individual author(s) and contributor(s) and not of MDPI and/or the editor(s). MDPI and/or the editor(s) disclaim responsibility for any injury to people or property resulting from any ideas, methods, instructions or products referred to in the content.